Assessing sinkhole activity in the Ebro Valley mantled evaporite karst using advanced DInSAR

Jorge Pedro Galve (1)*, Carmen Castañeda (2), Francisco Gutiérrez (1) and Gerardo Herrera (3)

(1) Departamento de Ciencias de la Tierra, Universidad de Zaragoza, C/Pedro Cerbuna 12, 50009 Zaragoza, Spain. E-mail: jpgalve@unizar.es (J.P.G.); fgutier@unizar.es (F.G.)

* Corresponding author's address: Departamento de Ciencias de la Tierra, Universidad de Zaragoza, C/Pedro Cerbuna 12, 50009 Zaragoza, Spain

E-mail: jpgalve@unizar.es (J.P.G.);

Tel.: +34 653 606226; Fax: +34 976 761106.

(2) Estación Experimental de Aula Dei, EEAD-CSIC, P.O. Box 13034, 50080 Zaragoza; E-mail: ccastaneda@eead.csic.es (C.C.)

(3) Geo Geohazards InSAR laboratory (InSARlab), Geological Survey of Spain (IGME), C/. Alenza 1, 13 28003, Madrid,Spain. E-mail: g.herrera@igme.es (G.H.)

Abstract

Sinkholes in karst areas may cause subsidence damage in transportation infrastructures, demolition of buildings and even the loss of human lives when they occur in a catastrophic way. Differential Interferometry (DInSAR) is a promising technology for detecting and characterizing sinkholes, as well as for reducing the associated risk when combined with other sources of data such as a sinkhole inventory. In this work, the usefulness of InSAR techniques and data for sinkhole risk management have been

analyzed through the comparison of three DInSAR-derived velocity maps with a comprehensive sinkhole inventory in the Ebro Valley, NE Spain. The DInSAR maps have contributed to improve the sinkhole inventory in different ways: (1) detection of non-inventoried sinkholes; (2) revision of sinkhole areas previously classified as inactive as active; (3) refinement of underestimated sinkhole boundaries. The obtained results suggest that DInSAR products are suitable for analyzing active dissolution-induced subsidence. The application of these techniques may help in recognizing and better characterizing previously unknown karst subsidence problems and in preventing personal and property losses. However, the analysis reveals that the available DInSAR maps combined overlook about 70% of the previously mapped active sinkholes mainly due to decorrelation.

Keywords: karst subsidence; SBAS; SPN; ERS; Envisat; ALOS

1. Introduction

Subsidence sinkholes are closed depressions commonly generated by subsurface dissolution of soluble rocks and the downward displacement of the overlying materials and the ground surface (Waltham et al., 2005). Three main subsidence mechanisms may operate independently or jointly: sagging, collapse, suffusion (Gutiérrez et al., 2008a; Cooper and Gutiérrez, 2013). The settlement of the land surface associated with sinkholes, regardless of the subsidence mechanism, may cause severe damage in any human structure borne by the undermined sediments. For the latest reviews on sinkhole related damage, see introduction section in Guerrero et al. (2008), Table 1 in Gutiérrez et al. (2009) and supplementary material in Galve et al. (2012). Collapse sinkholes related to the failure of cavity roofs may occur catastrophically and cause personal

losses. These rapid sinkholes may directly engulf buildings or people (e.g. De Bruyn and Bell, 2001) and lead to fatal accidents when they form in transportation routes. Previous investigations document slow ground subsidence (creep) preceding sudden collapse, suggesting that the occurrence of these highly dangerous phenomena might be anticipated through the detection of precursory displacements (e.g. Ferretti et al., 2004; Nof et al., 2013).

The avoidance of the existing sinkholes and the areas more prone to new sinkhole occurrences is usually the most cost-effective mitigation option (Cooper and Calow 1998; Gutiérrez, 2010). This preventive strategy is commonly based on the production of cartographic sinkhole inventories and susceptibility and hazard models derived from them (e.g. Galve et al., 2009a, 2011). However, sinkhole mapping is frequently a difficult task due to factors like the obliteration of the geomorphic expression of the depressions by anthropogenic and natural processes. Moreover, there is frequently a high uncertainty regarding the activity of the existing subsidence sinkholes. It is desirable to discriminate which are the active sinkholes and obtain information on their kinematics: (1) deformation regime (continuous, episodic or a combination of both); (2) subsidence rate; (3) spatial variability of the deformation pattern, including the precise limits of the area affected by ground motion. The assessment of the activity of sinkholes is usually based on qualitative data, like the freshness vs. degradation state of the depressions, the presence of recent surface deformation features or damaged structures. The application of traditional geodetic methods over large areas is not practical due to the dispersed and localized nature of the karst subsidence process.

Since the early 2000s (e.g. Baer et al, 2002), Differential Interferometric Synthetic Aperture Radar (DInSAR) techniques have opened promising and innovative prospects in sinkhole investigation. The use of SAR interferometry for the study of dissolution-induced subsidence was first applied along the Israeli Dead Sea shores (Derauw and Moxhet, 1996a, b; Cornet et al., 1997; Derauw, 1999; Baer et al., 2002). Subsequently, DInSAR studies have also been developed in karst areas of Germany, Italy, Jordan, Spain and USA. These works document: (1) gradual settlement in areas affected by sinkholes (Abelson et al., 2003; Al-Fares, 2005; Castañeda et al., 2009, 2011; Rucker et al., 2013); (2) displacements preceding the catastrophic collapse of cavities (Ferretti et al., 2000, 2004) or human structures underlain by karstified sediments (Closson et al., 2005, 2010); and (3) the relationships between karst subsidence and its triggering factors, such as earthquake shaking (Closson et al., 2010). Gutiérrez et al. (2011) presented a review of the abovementioned works and a research based on the combination of DInSAR displacement maps with conventional geomorphological methods, Ground Penetrating Radar (GPR) and trenching in the Ebro Valley (NE Spain). Dahm et al. (2010) combined geophysical data sets with InSAR-derived subsidence rates obtained by Schäffer (2009) in Hamburg, Germany. Paine et al. (2012) applied ALOS interferograms to guide site-specific gravimetric investigations over large sinkholes (90 to 200 m in diameter) related to deep-seated dissolution of salt in Texas, USA. The subsidence areas and rates (up to 30 mm/yr) generally matched previous data obtained by geodetic surveys. Since 2007, the availability of high resolution data and the improvement of DInSAR techniques and computing processes, make advanced-DInSAR (PS, SBAS) a promising technique even in areas that may pose temporal decorrelation limitations. This paper evaluates the capability of SAR data with different wavelengths and advanced DInSAR techniques to overcome some of the constraints

identified in previous works related to sinkhole activity: 1) the general limited coherence in agricultural areas and specially the frequent atmospheric noise in the study area (Castañeda et al., 2011), 2) insufficient spatial resolution to detect most of the active karst features (Castañeda et al., 2009); and 3) the restricted measurable deformation range that determine the identification of the active sinkhole according to their subsidence rates. Three DInSAR velocity maps are compared with a comprehensive sinkhole inventory in a sector of the Ebro Valley to analyze (1) the improvements and limitations of the more recently developed DInSAR products; (2) the contribution of the new data in active sinkhole detection and characterization; and (3) the implications for sinkhole risk management. Additionally, areas affected by subsidence identified using DInSAR that were not previously inventoried, were surveyed to semi-quantitatively assess sinkhole-related damage on human structures.

2. Study area

2.1 Geological setting

The investigation is focused on the mantled evaporite karst of Zaragoza metropolitan area, located in the middle reach of the Ebro Valley, NE Spain (Fig. 1a and b). The bedrock in this sector of the Ebro Cenozoic Basin consists of sub-horizontally lying evaporites of the Zaragoza Gypsum Formation (Quirantes, 1978). Secondary gypsum is the dominant rock type in outcrop and highly soluble halite and glauberite units up to 70 m and 30 m thick, respectively, occur a few tens of meters beneath the surface (Salvany et al., 2007; Salvany, 2009; Guerrero et al., 2013). This area is particularly prone to the development of sinkholes, especially those sectors where the evaporitic bedrock is covered by Quaternary alluvium (Galve et al., 2009b and references therein). It is regarded as the area in Europe with greatest economic losses related to evaporite

dissolution-induced subsidence (Gutiérrez et al., 2008b; Galve et al., 2009b). Moreover, this is one of the karst regions in the world where subsidence phenomena and their environmental implications have been more profusely investigated, (Galve et al., 2009b, 2012; Gutiérrez et al., 2011; Acero et al., 2013; Carbonel et al., 2013; Guerrero et al., 2013; Pueyo-Anchuela et al., 2013; Rodríguez-Tribaldos et al., in press). Regarding the application of radar interferometry, Zaragoza city area has been used in preliminary studies as a test site to explore the suitability of the DInSAR technique for the detection and monitoring of dissolution-induced subsidence (Castañeda, 2009).

The climate in the studied sector of the Ebro Valley is semiarid, with an average annual precipitation of 315 mm at Zaragoza Airport meteorological station. Rainfall distribution throughout the year is very irregular, with peaks in spring and autumn. Irrigation, which typically extends from March to September, constitutes around 90% of the recharge in the valley floor alluvium (Durán et al., 2005), enhancing the probability of occurrence of collapse sinkholes in some sectors (Benito and Gutiérrez, 1988; Gutiérrez et al., 2007; Galve et al., 2009c, 2011, 2012).

The study area, covering 40.8 km^2, is located upstream of Zaragoza city and coincides with the zone previously investigated by Galve et al. (2009b) from a geomorphological perspective. Sinkhole damage on roadways, buildings and other human structures is very common in this area. This is mainly related to the activity of pre-existing sinkholes filled by anthropogenic deposits and subsequently developed (e.g. Gutiérrez et al., 2009). Numerous buildings have been demolished and most of the main transportation structures require continuous remediation works or even relocation in sections affected by subsidence.

150

151 **2.2 Sinkhole inventory**

152 The detailed sinkhole inventory and geomorphological map used in this work were
153 produced by Galve et al. (2009b). This inventory is continuously updated incorporating
154 new sinkhole occurrences and additional information obtained from site investigations
155 applying multiple techniques (e.g. trenching, geophysics, boreholes; Gutiérrez et al.,
156 2011; Carbonel et al., 2013; Rodríguez-Tribaldos et al., in press). In order to assess
157 sinkhole activity, subsidence rate measurements have been gathered from available data
158 sources. These data were obtained through different procedures covering variable time
159 spans: topographic leveling profiles done by Soriano and Simón (2002); direct
160 measurements of the cumulative offset measured in scarps and man-made structures of
161 known age (Simón et al., 2008; Galve et al., 2009b); dating techniques using
162 geochronological methods (radiocarbon and optically stimulated luminescence) and
163 historical information (Gutiérrez et al., 2009, 2011; Carbonel et al., 2013). Note that
164 some measured subsidence rates correspond to minimum values that may be
165 significantly lower than the actual ones (e.g. vertical displacement measured in the
166 marginal sector of sinkholes). Moreover, estimated subsidence rates may not be directly
167 comparable because they may cover markedly different time spans. For instance, the
168 long-term subsidence rates derived from trenches go back to late Holocene periods,
169 whereas topographical profiles go back to the past decades.

170

171 The inventoried sinkholes have been classified into three main morphological and
172 genetic types (Galve et al., 2009b): large depressions, large collapse sinkholes and small
173 collapse sinkholes (Fig. 2):

- Large depressions correspond to broad and vaguely-edged basins up to 1138 m long and 3.6 m deep, typically with an elongated geometry showing a structurally-controlled preferred orientation (Fig. 2a). Castañeda et al. (2009), using InSAR data, detected progressive subsidence at rates of the order of several mm/yr in two sinkholes of the latter type.
- Large collapse sinkholes reach 114 m in diameter and 6.75 m in depth and have an average diameter of 43 m (Fig. 2b). Several decades ago, most of these depressions used to host permanent ponds. Nowadays they are mostly filled by man-made ground. Galve et al. (2009b) found surface evidence of active subsidence in 58% of these sinkholes. Subsidence rates of the order of cm/yr reported in some of these large collapses (cf. Simon et al., 2008 and Galve et al., 2009b) strongly suggest active deep-seated dissolution of salts (i.e. halite, glauberite).
- Small collapse sinkholes (Fig. 2c) are circular depressions up to 10 m across with scarped or overhanging edges that usually occur in a catastrophic way. To our knowledge, the deepest sudden collapse reported in the area reached 15.5 m in depth. InSAR data have significant limitations for detection of ground displacement associated with this type of sinkholes due to their reduced size and extremely fast subsidence (m/s). However, as mentioned above, previous works point out that collapse precursory displacements may be detected (Ferretti et al., 2004; Nof et al., 2013).

2.3 Damage surveys

Several detailed damage surveys were conducted in built-up areas affected by active subsidence identified in the DInSAR maps. The aim of these surveys was to identify

and semi-quantitatively assess sinkhole-related damage on buildings. There is no direct relationship between the detected subsidence and damage in buildings, because the latter are conditioned by multiple factors including the age and type of the structures, their foundation, the characteristics of the ground or the relative distribution between the sinkholes and the buildings (e.g. Mulas et al., 2003; Tomás et al., 2005; Herrera et al., 2009). However, these damage surveys help in the interpretation of the subsidence observed in the DInSAR displacement maps. The distribution and geometry of the deformation features depicted in the damage maps provide information on the spatial pattern of the subsidence (concavity of arcuate scarps and cracks orientation of the scarps, lowest point of sags). This evidence and the geomorphological and historical information help to elucidate whether the detected subsidence is related to an active sinkhole.

3. DInSAR processing

Differential Synthetic Aperture Radar Interferometry (DInSAR) is a microwave remote sensing technique that enables measuring surface displacement with sub-centimeter accuracy by subtracting the topographic phase from SAR interferograms (e.g. Massonnet and Feigl, 1998) by assuming that the scattering characteristics of the ground surface (ground nature and geometry) remain undisturbed (Rosen et al., 2000). Advanced Time-Series DInSAR techniques use two main approaches to measure ground displacement: the persistent scatterer approach (Ferretti et al., 2001) and the coherence approach (Berardino et al., 2002; Hooper et al., 2007). These techniques generally use a minimum number of SAR images to produce: (1) spatially dense maps with the average displacement rate of each persistent scatterer (PS) or coherent pixel along the line-of-sight (LOS) of the satellite; and (2) displacement time series of

224 individual points or pixels for which the phase information is preserved. These data
225 allow the identification of non-linear terrain motion on individual points or PS. The
226 minimum number of required SAR images depends upon the wavelength of the SAR
227 sensor, the time span of the analyzed period, the temporal lapse among SAR data
228 acquisitions and the ground deformation rate.
229
230 **3.1. SAR data**
231 Three DInSAR displacement rate maps were analyzed (Fig. 1b). They were produced
232 with archived data from three orbital SAR missions (Table 1); two sets of C-band data
233 and one set of L-band data. The oldest set corresponds to 27 ERS-1 and ERS-2 SAR
234 images acquired at 10:25 a.m. (mean local solar time) on descending orbits (track 237,
235 frame 2766) from 5 July 1995 to 21 December 2000. The second set includes 29
236 ENVISAT ASAR images acquired at 10.00 p.m. on ascending orbits (track 58, frame
237 829) from 2 May 2003 to 17 September 2010. The third dataset comprises 13 ALOS
238 PALSAR images acquired at 10.30 p.m. on ascending mode, HH polarization, covering
239 the period 12 February 2007 to 7 April 2010 (track 665, frame 820). The analyzed data
240 cover a period from 1995 to 2010, with a gap of about 2.3 years in 2000-2003. A total
241 of 69 acquisitions distributed throughout the different seasons were used; 22 were
242 acquired in summer, 22 in winter, 14 in spring and 11 in autumn.
243
244 **3.2. Advanced DInSAR processing**
245 The Small Baseline Subset (SBAS) approach was applied to process the 27 ERS-1/2
246 images by Castañeda et al. (2009). Details on the algorithm can be found in Berardino et
247 al. (2002). The 3 arc-second Digital Elevation Model (DEM) of the Shuttle Radar
248 Topography Mission (SRTM), with a 90-m pixel size and a vertical accuracy greater

than 16 m (Farr et al., 2007), was used to subtract the topographic phase of the interferograms. For the selection of the 74 high-signal-coherence multilook interferograms used in this investigation, maximum spatial and temporal baselines of 300 m and 1400 days, respectively, were considered in order to preserve coherence. The velocity map, hereafter SBAS-map, was generated at a ground resolution of about 90 m × 90 m and establishing a coherence threshold of 0.75 (Table S1, see online Supplementary Material). From the entire population of pixels with measurement data, only those with deformation rates >2 mm/yr were considered as ground affected by active deformation, which is the usual threshold for C-band data (Meisina et al., 2008; Bianchini et al., 2013).

The ENVISAT and ALOS SAR data were processed using the Stable Point Network (SPN) technique described by Crosetto et al. (2008). The SPN includes both the persistent and the distributed scatterers approaches, which were used depending upon the targeted phenomena and the availability of SAR images. The Spanish photogrammetric elevation model 'GISOleícola' produced from images taken in 1997-1998 was used to remove the topographic component of the interferometric phase. This model has a 20-m pixel size and vertical accuracy better than 5 m.

The SPN persistent scatterers approach was used to process the 29 ENVISAT ASAR images of the period 2003-2010. A coherence threshold of 0.46 was established (see Crosetto et al., 2008 for methodology) for the selection of persistent points (Table S1, see online Supplementary Material). The resulting velocity map, hereafter C-SPN-map, was obtained from a total of 61 interferograms. The ASAR dataset processing has maximum spatial and temporal baselines of 138 m and 1050 days, respectively. The

274 average LOS velocity and the LOS displacement time series of each PS were derived
275 from the Single Look Complex (SLC) ASAR images (full resolution). Points with
276 values >2 mm/yr were considered to be affected by actual deformation.
277
278 The 13 ALOS-PALSAR images from 2007-2010 were processed using the SPN
279 technique applying the distributed scatterer approach, generating 78 multilook (8 × 4)
280 interferograms. The PALSAR dataset processing has a maximum spatial baseline of 393
281 m and a maximum temporal baseline of 1150 days. The velocity map, hereafter L-SPN-
282 map, was produced at a ground resolution of about 25 m × 25 m and establishing a
283 coherence threshold of 0.40 (Table S1, see online Supplementary Material). In the L-
284 SPN-map, displacement rates >4 mm/yr are considered as indicative of actual ground
285 deformation, consistent with the threshold used by other authors (Sandwell et al., 2007;
286 Bianchini et al., 2013).
287
288 The density of measurement points (i.e. PS or pixels, according to the technique) in the
289 SBAS-, C-SPN- and L-SPN- maps are 26, 597 and 156 points/km^2, respectively. In the
290 three maps, the lowest density of points occurs in irrigated lands, whilst the highest
291 densities occur in urban and industrial zones. The density of measurement points for the
292 different land covers in each DInSAR map can be found in the online Supplementary
293 Material (Fig. S1).
294
295 The sinkhole inventory and the evidence of ground subsidence identified in the field
296 were used to assess the consistency and validity of the three velocity maps. The
297 deformation data in the L-SPN-map are systematically shifted towards negative values
298 (Fig. 3). The shift was corrected considering that the pixels in the L-SPN-map

coinciding with stable pixels in the SBAS-map should indicate no ground motion. The shift was calculated as the difference between (1) the mean deformation rate of the 1% "most stable" pixels of the SBAS-map (i.e. pixels with the lowest displacement rate) and (2) the average deformation rate of the pixels in the L-SPN-map coinciding with the selected stable SBAS pixels. The obtained shift (1 mm/yr) was then subtracted from each value of the deformation time series. The resulting L-SPN-map displays a general ground deformation pattern consistent with that of the SBAS- and C-SPN-maps. The main parameters of the DInSAR velocity maps are indicated in Table S1 (see online Supplementary Material).

4. Assessment of DInSAR velocity maps for sinkhole detection

The main results of the comparative analysis between the three DInSAR velocity maps (Fig. 4b, c and e) and the available sinkhole map (Fig. 4a) are featured below. The results are presented according to a multi-scale approach. A general analysis covering the entire study area (section 4.1) is followed by a site- and sinkhole-specific analysis (section 4.2). See Figure 4a for location of analyzed sites and sinkholes.

4.1. General analysis of the study area

The sinkhole map of the study area and the three DInSAR velocity maps are shown in Figure 4. The velocity maps suggest that most of the study area is stable, with 88.4% (SBAS-map), 94.4 % (C-SPN-map) and 97% (L-SPN-map) of the points indicating displacement rates below the range of the proposed deformation detection limits (Fig. 3). However, the three DInSAR maps consistently depict unstable areas with negative mean LOS displacement rates indicative of active subsidence, mostly coincident with mapped sinkholes (Fig. 4 and Table S2, see online Supplementary Material).

Ground motion measurements have been considered to be unambiguously related to sinkhole activity when they met the following requirements: (1) negative mean LOS displacement rate higher than the proposed stability thresholds; (2) the occurrence of a minimum of three subsidence points within the inventoried sinkhole area; (3) in large collapse sinkholes, ground motion values with a spatial arrangement consistent with the typical subsidence pattern of sinkholes (i.e. increasing subsidence rates towards the inner sector of the depressions). As an example, the latter spatial distribution of the subsidence kinematics can be recognized in the sinkhole illustrated in figure 5. The analysis has only focused on InSAR subsidence data recorded within known active sinkholes because the interpretation of false negatives or false positives is a intricate issue in the studied case. For example, the statistics on stable PSs and inactive sinkholes may be biased because most of the sinkholes defined as inactive are located in agricultural areas where InSAR data point coverage is very low. Moreover, in agricultural areas subsidence signs are difficult to detect and many of the inventoried sinkholes classified as inactive may be actually active. On the other hand, the InSAR points showing subsidence motion on confirmed active sinkholes do not generate ambiguity or errors.

According to the three aforementioned criteria, the SBAS-map provides subsidence data within 2 active sinkholes that represent 31% of the active sinkhole area in the cartographic inventory. The C-SPN-map detects 12 active sinkholes (45%) and 10 active sinkholes (48%) are detected in the L-SPN-map. Overall, the three DInSAR maps have permitted the detection of 14 out of 48 previously mapped active sinkholes, overlooking half of the area affected by active karst subsidence (i.e. 70% of the

previously mapped active sinkholes). DInSAR maps have been useful for (1) revising the category of two sinkholes previously classified as inactive (see Fig. 6; Table S2, see online Supplementary Material), (2) detecting two non-inventoried active subsidence areas where further investigations should be conducted, and (3) recognizing in the field surface evidence of ongoing subsidence in specific sectors of a large depression (see Section. 4.2.2, Sinkhole B2).

As expected, most of the detected active sinkholes are located in urban fabric whereas none of them have been detected in irrigated lands, due to the signal decorrelation in non-developed environments. Only in the case of residential areas located within the irrigated land could DInSAR maps detect sinkhole-related subsidence (see Fig. 7).

Regarding the detection of the different types of sinkholes, under favorable conditions, large active depressions can be identified with the applied DInSAR techniques (Castañeda et al., 2009). The L-SPN-map provides subsidence measurements in 7 out of 14 (50%) active large depressions and the C-SPN-map in 6 of them. The recognition of subsidence activity associated with large collapse sinkholes is more difficult due to their smaller size and higher subsidence rates. Subsidence rates in large collapses are usually higher than in large depressions and their detection is difficult due to decorrelation at their sinking centers. Maximum subsidence rates of 17 mm/yr measured in the current study with DInSAR are well below the settlement rates estimated in some of the most active collapse sinkholes of the study area (>50 mm/yr). Nevertheless, subsidence has been measured in 6 out of 34 (17%) active large collapse sinkholes with L-SPN- and C-SPN- maps. Monitoring these 6 specific sinkholes has been possible due to their adequate size (>2500 m^2), subsidence kinematics and land cover (urban fabric).

The C-SPN-map provided deformation measurements in the vicinity of a sudden collapse sinkhole 10 m across and 4 m deep occurred in 24 May 2006, next to the N-232 highway (Fig. 8). However, the recorded continuous subsidence rate (3 mm/yr) between May 2003 and September 2010, seems to be related to a sagging mechanism that was not altered by the sudden collapse of a cavity in the adjacent ground.

4.2. Analysis of representative sites

The analysis of two representative sites corresponding to industrial and urban contexts, respectively, illustrates the possibilities and limitations of the available DInSAR data to detect active sinkholes and assess subsidence kinematics in these settings. These contexts met two important factors: (1) the suitability of the land covers for the DInSAR technique; and (2) the great socio-economic impact of the sinkhole hazard in these areas, including high risk situations.

4.2.1. Site A. Industrial estates and areas adjacent to the N-232 highway

This site includes the sectors of the study area with the highest density of sinkholes; 20% of the area is affected by 11 active sinkholes. The Europa and El Portazgo industrial estates were built next to the N-232 highway on these sinkholes currently filled with anthropogenic deposits (Figs. 1c and 4a). These depressions used to host wetlands with ponds and flood-prone areas. Soon after construction, the buildings displayed conspicuous evidence of damage related to dissolution subsidence, most probably amplified by compaction of the natural sinkhole fill deposits and man-made fills (Galve et al., 2009b). Two catastrophic collapse sinkholes occurred in 1994 and 1999 (see Fig. 5 for the location of the latter) and progressive subsidence led to the

399 partial or total demolition of at least ten warehouses. Currently, multiple areas affected
400 by differential subsidence can be recognized, showing a close spatial correlation with
401 the obliterated karst depressions (Galve et al., 2009b). This site also includes a partially
402 developed strip of land situated just south of the N-232 highway. This sector has been
403 the focus of a detailed investigation integrating geomorphological mapping, trenching,
404 Ground Penetrating Radar (GPR) and previous DInSAR data (Gutiérrez et al., 2011).
405
406 Previously, only two active sinkholes out of 11 were clearly detected by the SBAS-map
407 (Castañeda et al., 2009). The new maps have increased the number of detected active
408 sinkholes (C-SPN-map) and the density of deformation points within them (C-SPN- and
409 L-SPN-map, cf. Table S2, see online Supplementary Material). In this site, the density
410 of measurement points, the detected sinkhole area and the negative LOS displacement
411 rates reach the highest values of the study area.
412
413 Sinkhole A1
414 This is a large compound sinkhole (uvala) covering about 0.2 km^2 with ill-defined edges,
415 partially due to topographic modifications related to human activity. The uvala
416 comprises eleven large collapse sinkholes, five areas dominated by sagging subsidence
417 and a small collapse sinkhole that occurred in 1994. A long-term subsidence rate of 0.8-
418 1 mm/yr was estimated in the southern marginal sector of the depression. This rate was
419 calculated using radiocarbon-dated late Holocene deposits exposed in a trench and
420 assuming an aggradation rate equivalent to the subsidence rate (Gutiérrez et al., 2011)
421 (Fig. 9a). None of the DInSAR velocity maps provide displacement data in the trenched
422 zone, corresponding to abandoned crop fields with natural vegetation.
423

The sinkhole is mostly occupied by industrial wasteland and yields a moderate density of measurement points in the three DInSAR maps. The maximum and average LOS displacement rates recorded in the C-SPN- and L-SPN- maps are -10 mm/yr and -3 mm/yr, respectively. A maximum cumulative LOS displacement of -71 mm over 7.4 years has been measured by the C-SPN-map. The E-W profile constructed with the LOS displacement rates of the C-SPN-map illustrates the differential settlement recorded in this composite sinkhole (Fig. 9c). Most of the DInSAR subsidence points are located within the limits of the previously mapped sinkhole (Galve et al., 2009b). However, the L-SPN-map indicates active subsidence beyond the western edge of the mapped sinkhole in a roundabout of the N-232 motorway, indicating that it may extend over a larger area (Fig. 9a).

Sinkholes A2 and A3

It is interesting to compare these two large collapse sinkholes with similar characteristics: (1) Both cover an area larger than the minimum size for detectable sinkholes with our data (around 2500 m^2, cf. section 4.1); and (2) are located almost entirely in the same land cover; the N-232 motorway and the adjacent paved surfaces (Fig. 10). Sinkhole A2 is a well-known sub circular collapse structure about 100 m in diameter that causes continuous subsidence in the N-232 motorway, requiring periodic re-leveling and re-asphalting. This sinkhole also affects a warehouse located on its northern edge. Centimeter-sized scarps developed in the motorway within a few months after re-asphalting reveal the high subsidence rates in this sinkhole, in which Simón et al. (2008), based on periodic topographic profiling, reported maximum vertical displacement rates of 60-110 mm/yr. The very low density of measurement points in this sinkhole can be attributed to the high deformation rate and the frequent surface

changes related to the repair works. Only one deformation point was recorded within this sinkhole in the C-SPN-map (Fig. 10). The adjacent sinkhole A3, located to the SE, was first described by Gutiérrez et al. (2011) and currently is expressed as a shallow pothole in the road. Subsidence in this sinkhole is recorded by 9 PS points in the C-SPN-map. A maximum cumulative C-SPN LOS displacement of -67 mm has been measured in the center of the depression between May 2003 and September 2010. The SBAS- and L-SPN-map have not detected deformation in this sinkhole. Although sinkhole A2 is larger than sinkhole A3, the latter has been detected by the C-SPN-map probably because of its higher coherence and amplitude stability derived from its slower subsidence and less frequent repair works.

4.2.2. Site B. Valdefierro suburb

Valdefierro suburb is located on the southwestern sector of Zaragoza city, astride two terrace levels of the Ebro River underlain by slightly indurated alluvium. This is the sector of the city itself most severely affected by sinkhole damage. Four large active sinkholes have been mapped using geomorphological procedures and dissolution-induced ground settlement has led to the demolition of at least four buildings in the last few decades.

Even though the DInSAR measurement point density shows the highest value due to the urban fabric, only 2 inventoried sinkholes were detected with the C-SPN-map, and none of them with the SBAS- and L-SPN-maps (Table S2 , see online Supplementary Material).

None of the maps detect ground subsidence in a complex sagging and collapse sinkhole with surface evidence of recent deformation located in a periurban wasteland (Carbonel et al., 2013; Rodríguez-Tribaldos et al., in press), probably due to surface changes related to the accumulation of rubble and vegetation.

Sinkhole B1

This is an elliptical depression about 125 m long affecting an Ebro River terrace and an inset flat-bottom infilled valley (Fig. 11). The floor, partially filled with anthropogenic deposits, shows a nested fresh-looking collapse a few meters across. The location of the sinkhole edges is highly uncertain due to topographic changes related to the accumulation of man-made deposits and construction. Subsidence activity has caused conspicuous damage in a block of apartments built on the southeastern sector of the sinkhole: (1) cracking on the wall facing the sinkhole; (2) settlement in the backyards; (3) the collapse of a ditch and its retaining wall. Local subsidence rates of 20-30 mm/yr have been estimated observing the maximum vertical displacement of the backyard gardens and the age of the property. These values may be related to the contribution of both karstic subsidence and compaction of the thick anthropogenic deposits underlying the backyards. The C-SPN-map provides subsidence measurements in five points located in the external zone of the depression, with LOS displacement rates of up to -9 mm/yr, three of them located on human structures and the other two on wasteland. It seems that subsidence rates in the central sector of the depressions are well above the maximum detectable velocity.

Sinkhole B2

This is a large complex sinkhole covering about 38,600 m^2, identifiable in old aerial photographs as an anomalous widening of a flat-bottom valley carved in a terrace (Fig. 12). The depression has been filled and developed since the 1950s, mostly with low-rise buildings. Soriano and Simón (2002) measured local subsidence rates of 21-24 mm/yr and Galve et al. (2009b) mapped an active sub circular depression approximately 50 m in diameter, underestimating the actual extent of the area affected by active subsidence.

Subsidence recorded in the C-SPN-map is restricted to the western sector of the depression, with maximum LOS displacement rates of -8 mm/yr. Ground settlement in this portion of the sinkhole, consistent with the mapped structural damage, passed unnoticed to us before the production of the DInSAR velocity maps. Figure 12 shows the measurement points and the subsidence damage map, produced following the ranking scheme proposed by Cooper (2008). Some of the damage observed in the façades of the buildings and paved surfaces are illustrated in Figure 13. Both the surface evidence of deformation and the damage map, indicate that subsidence increases towards the eastern sector of the sinkhole, where two buildings have been demolished (Fig. 12). In this area no deformation data have been recorded, suggesting that the displacement rates could be below the DInSAR detection limit.

5. Discussion and conclusions

5.1. Detection of active sinkholes using DInSAR techniques

The previously produced and analyzed SBAS-map (Castañeda et al., 2009), with a pixel size of ~90 m, is compared with the two new velocity maps (C-SPN- and L-SPN-map) with higher spatial resolution (Table S1, see online Supplementary Material). Both C- and L- SPN-maps have increased the density of measurement points by 23 and 6 times,

522 respectively (Table S2, see online Supplementary Material), resulting in the recognition
523 of a higher number of active sinkholes and detection of smaller subsidence features.
524
525 Subsidence zones detected in the DInSAR maps show a good spatial correlation with
526 previously mapped sinkholes. These unstable zones largely correspond to active
527 sinkholes filled with anthropogenic deposits, and subsequently used for the construction
528 of human structures, acting as adequate reflective surfaces for the radar signals.
529 However, the proportion of inventoried active sinkholes captured in the DInSAR
530 velocity maps is below 25%. A total of 2, 12 and 10 sinkholes out of the 48 mapped
531 sinkholes have been detected in the SBAS-, C-SPN- and L-SPN-map, respectively. The
532 proportion of sinkholes larger than 100 m in length has increased from 10% in the
533 SBAS-map, to 35% and 40% in the C-SPN- and L-SPN-map, respectively. Sinkholes
534 smaller than 100 m across have been captured only in the C-SPN-map (4 out of 28).
535 Moreover, the integration of the three DInSAR maps has permitted the identification of
536 30% of the active sinkholes (14 out of 48), which represent a low proportion of the
537 previously mapped active sinkholes using traditional methods.
538
539 DInSAR velocity maps have been useful for: (1) re-classifying two sinkholes as active
540 (see Fig. 6; Table S2, see online Supplementary Material); (2) detecting two non-
541 inventoried active subsidence areas where further investigations should be made; (3)
542 recognizing subsidence spatial variability within particular sinkholes (sinkholes A1 and
543 B2; Figs. 9 and 12); (4) redefining the underestimated active boundary of an active
544 sinkhole (Figs. 5 and 9).
545

546 DInSAR constrains for sinkhole activity mapping in the study area are threefold: (1)
547 Decorrelation in irrigated lands. Sinkhole-related subsidence was not detected away
548 from urban areas. Particularly on irrigated lands that cover approximately 60% of the
549 analyzed area. (2) Minimum sinkhole detectable area. The minimum detectable sinkhole
550 area is approximately 2500 m^2. Consequently, small collapse sinkholes and a significant
551 proportion of the large collapse sinkholes could not be detected; (3) DInSAR detection
552 limits. The datasets available for this study were suitable for measuring subsidence rates
553 as high as 17 mm/yr. Therefore, our velocity maps overlook faster subsidence rates
554 characteristic of some collapse sinkholes, reaching up to 110 mm/yr (cf. Simón et al.,
555 2008; Galve et al., 2009b). Areas affected by low subsidence rates of the order of 1
556 mm/yr, as revealed by trenching investigations (Gutiérrez et al., 2011), cannot be
557 detected since they fall within the adopted stability thresholds.
558
559 The assessment of sinkhole activity with DInSAR techniques could be improved
560 substantially through: (1) the selection of those SAR images that maximize ground
561 surface coherence and minimize atmospheric disturbances; (2) the acquisition of high
562 resolution SAR images from TerraSAR-X or COSMO-SkyMed satellites; (3) the
563 analysis of short-temporal interferograms generated with high-resolution SAR and
564 elevation data to partially overcome the restrictions posed by small collapse sinkholes
565 affected by high subsidence rates. This approach was followed by Nof et al. (2013) in
566 the Dead Sea, Israel, providing information on the subsidence kinematics during the
567 pre-collapse and post-collapse stages of small collapse sinkholes; (4) installing artificial
568 corner reflectors in selected decorrelated areas with known subsidence (Crosseto et al.,
569 2013); (5) combining DInSAR methods with other geodetic techniques (e.g. differential
570 GPS, precise leveling) and deformation monitoring (e.g. tiltmeter arrays, horizontal

extensiometers). The latter approaches have to be restricted to specific sinkholes, which can be previously identified and selected on the basis of regional DInSAR analyses.

5.2. Comparison of traditional methods and DInSAR for sinkhole activity mapping

Mapping active sinkholes by means of traditional geomorphological techniques is a costly and time-consuming task that requires a significant effort including intensive field surveys. DInSAR, under favorable conditions, may provide accurate sinkhole-related displacement data with high spatial and temporal resolution over large areas. This information may be obtained remotely at a relatively low cost and in a brief period of time. However, in our study area, traditional methods, including geomorphological mapping and historical data compilation, allow the construction of a much more comprehensive sinkhole inventory. The combination of the available multi-sensor DInSAR maps overlooks about 70% of the previously mapped sinkholes, which should be considered as potentially unstable areas. Moreover, a sound interpretation of DInSAR ground displacement data needs to be based on a detailed geological background on the study area. This is clearly illustrated by the case of the Ebro Valley, where the insight on the evaporite karst gathered over the last decades has been essential in the interpretation of the DInSAR velocity maps and the assessment of their performance. Consequently, DInSAR methods should not be considered as an alternative to classical mapping methods, but a highly useful complementary approach. This is specially the case in sectors not affected by coherence loss, where DInSAR may provide information on the spatio-temporal evolution patterns of subsidence, helping to refine the mapped boundaries of active sinkholes. Moreover the acquisition of these ground subsidence data using traditional geodetic methods may not be feasible in some

595 cases due to multiple factors, including economic and time constraints, as well as
596 vandalism or access restrictions.
597
598 In agricultural areas active sinkholes are very difficult to identify due to the loss of
599 coherence produced by vegetation and surface changes. The identification of these
600 sinkholes is only useful when combined with other sources of information (e.g. historic
601 aerial photographs, interviews with local people) and geotechnical site investigations
602 (e.g. geophysical surveys, trenching, boreholes) (Gutiérrez et al., 2011; Carbonel et al.,
603 2013).
604
605 In urban areas, the higher density of DInSAR measurement points may help to rapidly
606 recognize unstable areas that could be related to active sinkholes, where damage
607 surveys and monitoring programs could be undertaken. These surveys provide indirect
608 evidence of the spatial distribution and intensity of the subsidence phenomena and may
609 be used as a preliminary and independent source of data to assess the validity and
610 performance of the DInSAR maps.
611
612 The analysis presented above indicates that sinkhole activity mapping requires the
613 combination of multiple techniques, whose prominence depends on multiple factors like
614 the extent of the study area, the type of sinkholes and land covers, the goal of the
615 investigation or the available budget. In any case, it is desirable to explore multiple
616 independent lines of evidence and assess their consilience, in order to build a robust
617 model; for instance, obtaining subsidence rates using ground- and satellite-based
618 techniques and compare them with rates estimated from dated deformed human and
619 geological markers.

620

621 **5.3 Implications for sinkhole risk management**

622 The vast majority of the subsidence damage in the study area occurs within the
623 boundaries of previously existing sinkholes. Thus, ground motion is mostly related to
624 continuous long-sustained subsidence activity in large depressions and collapse
625 sinkholes (Figs. 5-7, 9-13) or less frequently to the sudden occurrence of small collapse
626 sinkholes, commonly spatially associated with large sinkholes (Fig. 8). Consequently,
627 the identification and characterization of the pre-existing sinkholes, including those
628 obliterated by human activity, is the critical step for risk mitigation in the area (Galve et
629 al., 2009b; Gutiérrez et al., 2011). The DInSAR velocity maps analyzed in this work, in
630 spite of their limitations, support the quality of the available sinkhole inventory and
631 contribute to improve it. The potential of DInSAR techniques to upgrading sinkhole
632 inventories is expected to increase significantly using high resolution SAR sensors with
633 shorter revisiting time provided by new satellite constellations. Moreover, in the near
634 future DInSAR may help to anticipate the development of catastrophic collapse
635 sinkholes through the detection of precursory deformation, which might constitute the
636 basis for an early warning system (Ferreti et al., 2004; Nof et al., 2013).

637

638 The results obtained in the Ebro Valley evaporite karst strongly suggest that InSAR
639 could be an adequate and cost-effective technology to explore evaporite dissolution
640 subsidence in other regions of the world, particularly urban areas that offer higher
641 coherence. For instance, some large cities in Europe like Hamburg (Dahm et al., 2010),
642 Paris (Thierry et al., 2009) and Madrid (Gutiérrez et al., 2008b) suffer from subsidence
643 damage related to evaporite karstification. Particularly severe damage has been reported
644 in smaller cities underlain by cavernous evaporites like Ripon and Darlington, UK

(Cooper, 1995), Calatayud, Spain (Gutiérrez and Cooper, 2002), Barzai and Pasvalys, Lithuania (Paukstys et al., 1999) and Dzerzhinsk, Russia (Koutepov et al., 2008). It may be also interesting to explore the suitability of this technique in mantled carbonate karst areas, were slow subsidence related to suffusion processes and possibly sagging preceding collapse might be resolved with high-resolution InSAR measurements. In this regard, many cities all over the world could be analyzed such as Guilin and other metropolises in southeastern China (Lei et al., 2002), the metropolitan area of Moscow, Russia (Tolmachev and Leonenko, 2011) or the urban areas in the West-Central Florida, USA (Aurit et al., 2013) just to give some examples. The application of these methods may help to recognize previously unknown karst subsidence problems and prevent personal and property losses.

Acknowledgments

We wish to thank five anonymous reviewers for their helpful comments. This research has been funded by the Spanish national projects CGL2010-16775 and AGL2012-40100 (Ministerio de Ciencia e Innovación and FEDER), the Regional projects 2012/GA-LC-021 and 2012/GA LC 036 (DGA-La Caixa) and the European Interreg IV B SUDOE project DO-SMS-SOE1/P2/F157. Jorge Pedro Galve has been contracted under the DGA-La Caixa project and the contract of Carmen Castañeda is co-funded by ESF. SPN maps (derived from ENVISAT and ALOS data) were produced by Altamira Information S.L. (Spain). The 2009 orthoimages and the 5 x 5 m LiDAR DEM are products of the National Geographic Institute of Spain (Instituto Geográfico Nacional) available in: http://centrodedescargas.cnig.es/CentroDescargas/index.jsp.

References

670 Abelson, M., Yechieli, Y., Crouvi, O., Baer, G., Wachs, D., Bein, A., Shtivelman, V.,
671 2003. Collapse-sinkholes and radar interferometry reveal neotectonics concealed
672 within the Dead Sea basin. Geophysical Research Letters 30, 2-5.
673 Acero, P., Gutierrez, F., Galve, J.P., Auqué, L.F., Carbonel, D., Gimeno, M.J., Gómez,
674 J.B., Asta, M.P., Yechieli, Y., 2013. Hydrogeochemical characterization of an
675 evaporite karst area affected by sinkholes (Ebro Valley, NE Spain). Geologica
676 Acta 11, 389-407.
677 Al-Fares, R., 2005. The Utility of Synthetic Aperture Radar (SAR) Interferometry in
678 Monitoring Sinkhole Subsidence: Subsidence of the Devil's Throat Sinkhole Area
679 (Nevada, USA). In: Beck, B.F. (Ed.), Proceedings of the 10th Multidisciplinary
680 Conference on Sinkholes and the Engineering and Environmental Impacts of Karst.
681 San Antonio, Texas, US, pp. 541 - 547.
682 Aurit, M.D., Peterson, R.O., Blanford, J.I., 2013. A GIS Analysis of the Relationship
683 between Sinkholes, Dry-Well Complaints and Groundwater Pumping for Frost-
684 Freeze Protection of Winter Strawberry Production in Florida. PloS one 8, e53832.
685 Baer, G., Schattner, U., Wachs, D., Sandwell, D., Wdowinski, S., Frydman, S., 2002.
686 The lowest place on earth is subsiding - An InSAR (interferometric synthetic
687 aperture radar) perspective. Geological Society of America, Bulletin 114, 12-23.
688 Benito, G., Gutierrez, M., 1988. Karst in gypsum and its environmental impact on the
689 Middle Ebro Basin (Spain). Environmental Geology and Water Sciences 12, 107-
690 111.
691 Berardino, P., Fornaro, G., Lanari, R., Sansosti, E., 2002. A new algorithm for surface
692 deformation monitoring based on small baseline differential SAR interferograms.
693 IEEE Transactions on Geoscience and Remote Sensing 40, 2375-2383.

694 Bianchini, S., Herrera, G., Mateos, R.M., Notti, D., García, I., Mora, O., Moretti, S.,
695 2013. Landslide Activity Maps Generation by Means of Persistent Scatterer
696 Interferometry. Remote Sensing 5, 6198-6222.
697 Carbonel, D., Rodríguez, V., Gutiérrez, F., McCalpin, J.P., Linares, R., Roqué, C.,
698 Zarroca, M., Guerrero, J., Sasowsky, I., 2013. Evaluation of trenching, Ground
699 Penetrating Radar (GPR) and Electrical Resistivity Tomography (ERT) for
700 sinkhole characterization. Earth Surface Processes and Landforms 39, 214-227.
701 Castañeda, C., 2009. Zaragoza, Spain. In: Caper, R., Marsh, S. (Eds.), The Terrafirma
702 Atlas. A compendium of results produced by the European Space Agency GMES
703 Service Element Project Terrafirma 2003-2009. ESRIN Contract 19366/05/I-EC,
704 pp. 40.
705 Castañeda, C., Gutiérrez, F., Manunta, M., Galve, J.P., 2009. DInSAR measurements of
706 ground deformation by sinkholes, mining subsidence, and landslides, Ebro River,
707 Spain. Earth Surface Processes and Landforms 34, 1562-1574.
708 Castañeda, C., Pourthié, N., Souyris, J.-C., 2011. Dedicated SAR interferometric
709 analysis to detect subtle deformation in evaporite areas around Zaragoza, NE
710 Spain. International Journal of Remote Sensing 32, 1861-1884.
711 Closson, D., Karaki, N.A., Klinger, Y., Hussein, M.J., 2005. Subsidence and Sinkhole
712 Hazard Assessment in the Southern Dead Sea Area, Jordan. Pure and Applied
713 Geophysics 162, 221-248.
714 Closson, D., Karaki, N.A., Milisavljevic, N., Hallot, F., Acheroy, M., 2010. Salt-
715 dissolution-induced subsidence in the Dead Sea area detected by applying
716 interferometric techniques to ALOS Palsar Synthetic Aperture Radar images.
717 Geodinamica Acta 23, 65-78.

718 Cooper, A.H., 1995. Subsidence hazards due to the dissolution of Permian gypsum in
719 England: Investigation and remediation. In: Beck, B.F. (Ed.), Karst Geohazards.
720 Engineering and Environmental Problems in Karst Terrane, Proceedings of the
721 Fifth Multidisciplinary Conference on Sinkholes and the Environmental Impacts
722 of Karst. Balkema, Gatlingburg, Tennessee, pp. 23-29.
723 Cooper, A.H., 2008. The classification, recording, databasing and use of information
724 about building damage caused by subsidence and landslides. Quarterly Journal of
725 Engineering Geology and Hydrogeology 41, 409-424.
726 Cooper, A.H., Calow, R.C., 1998. Avoiding gypsum geohazards: Guidance for planning
727 and construction. British Geological Survey, Nottingham, UK, 57 pp.
728 Cooper, A.H., Gutiérrez, F., 2013. Dealing with gypsum karst problems: hazards,
729 environemental issues and planning. In: Shroder, J., Frumkin, A. (Eds.), Treatise
730 on Geomorphology. Vol. 6 Karst Geomorphology. Academic Press, San Diego,
731 CA, pp. 451-462.
732 Cornet, Y., Doulliez, J.-Y., Moxhet, J., Closson, D., Kourgli, A., Ozer, P., Ozer, A.,
733 Derauw, D., 1997. Use of ERS tandem data to produce digital elevation models by
734 interferometry and study land movements by differential interferometry in
735 Calabria and Jordan. ERS symposium on space at the service of our environment
736 N°3, Florence, Italy (14/03/1997).
737 Crosetto, M., Biescas, E., Duro, J., Closa, J., Arnaud, A., 2008. Generation of advanced
738 ERS and Envisat interferometric SAR products using the Stable Point Network
739 technique. Photogrammetric Engineering and Remote Sensing 74, 443.
740 Crosetto, M., Gili, J.A., Monserrat, O., Cuevas-González, M., Corominas, J., Serral, D.,
741 2013. Interferometric SAR monitoring of the Vallcebre landslide (Spain) using
742 corner reflectors. Nat. Hazards Earth Syst. Sci. 13, 923–933.

743 Dahm, T., Kühn, D., Ohrnberger, M., Kröger, J., Wiederhold, H., Reuther, C.-D.,
744 Dehghani, A., Scherbaum, F., 2010. Combining geophysical data sets to study the
745 dynamics of shallow evaporites in urban environments: application to Hamburg,
746 Germany. Geophysical Journal International 181, 154-172.
747 De Bruyn, I.A., Bell, F.G., 2001. The occurrence of sinkholes and subsidence
748 depressions in the far West Rand and Gauteng province, South Africa, and their
749 engineering implications. Environmental and Engineering Geoscience 7, 281-295.
750 Derauw, D., 1999. Synthetic Aperture Radar phasimetry: theory and applications
751 (Phasimétrie par Radar à Synthèse d'Ouverture: théorie et applications). PhD
752 Thesis. University of Liege, Belgium. 118 pp. (in French).
753 Derauw, D., Moxhet, J., 1996a. Preliminary results of Tandem SAR interferometry and
754 differential interferometry over the Dead Sea area. Fringe'96, ESA Workshop on
755 Applications of ERS SAR Interferometry. Remote Sensing Laboratories,
756 University of Zurich, September 30th - October 2nd, Switzerland.
757 Derauw, D., Moxhet, J., 1996b. Multiple Image SAR Interferometry. Fringe'96, ESA
758 Workshop on Applications of ERS SAR Interferometry. Remote Sensing
759 Laboratories, University of Zurich, September 30th - October 2nd, Switzerland.
760 Digital.
761 Durán, J.J., Garrido, E., García, M., 2005. Trabajos técnicos para la aplicación de la
762 Directiva Marco del Agua en materia de Aguas Subterráneas. Caracterización
763 Adicional Aluvial del Ebro-Zaragoza, 112 pp.
764 Farr, T.G., Rosen, P.A., Caro, E., Crippen, R., Duren, R., Hensley, S., Kobrick, M.,
765 Paller, M., Rodriguez, E., Roth, L., Seal, D., Shaffer, S., Shimada, J., Umland, J.,
766 Werner, M., Oskin, M., Burbank, D., Alsdorf, D., 2007. The Shuttle Radar
767 Topography Mission. Reviews of Geophysics 45 (2), 1-33.

768 Ferretti, A., Ferrucci, F., Prati, C., Rocca, F., 2000. SAR analysis of building collapse
769 by means of the permanent scatterers technique. Geoscience and Remote Sensing
770 Symposium, 2000. Proceedings. IGARSS 2000. IEEE 2000 International, pp.
771 3219-3221.
772 Ferretti, A., Prati, C., Rocca, F., 2001. Permanent scatterers in SAR interferometry.
773 IEEE Transactions on Geoscience and Remote Sensing 39, 8-20.
774 Ferretti, A., Basilico, M., Novali, F., Prati, C., 2004. Possibile utilizzo di dati radar
775 satellitari per individuazione e monitoraggio di fenomeni di sinkholes. In: Nisio, S.
776 (Ed.), Stato dell'arte sullo studio dei fenomeni di sinkholes e ruolo delle
777 amministrazioni statali e locali nel governo del territorio, APAT, Roma, pp. 415-
778 425.
779 Galve, J.P., Gutiérrez, F., Remondo, J., Bonachea, J., Lucha, P., Cendrero, A., 2009a.
780 Evaluating and comparing methods of sinkhole susceptibility mapping in the Ebro
781 Valley evaporite karst (NE Spain). Geomorphology 111, 160-172.
782 Galve, J.P., Gutiérrez, F., Lucha, P., Bonachea, J., Remondo, J., Cendrero, A., Gutiérrez,
783 M., Gimeno, M.J., Pardo, G., Sánchez, J.A., 2009b. Sinkholes in the salt-bearing
784 evaporite karst of the Ebro River valley upstream of Zaragoza city (NE Spain).
785 Geomorphology 108, 145-158.
786 Galve, J.P., Gutiérrez, F., Lucha, P., Guerrero, J., Bonachea, J., Remondo, J., Cendrero,
787 A., 2009c. Probabilistic sinkhole modelling for hazard. Earth Surface Processes
788 and Landforms 34, 437-452.
789 Galve, J.P., Remondo, J., Gutiérrez, F., 2011. Improving sinkhole hazard models
790 incorporating magnitude – frequency relationships and nearest neighbor analysis.
791 Geomorphology 134, 157-170.

792 Galve, J.P., Gutiérrez, F., Guerrero, J., Alonso, J., Diego, I., 2012. Optimizing the
793 application of geosynthetics to roads in sinkhole-prone areas on the basis of
794 hazard models and cost-benefit analyses. Geotextiles and Geomembranes 34, 80-
795 92.
796 Guerrero, J., Gutiérrez, F., Bonachea, J., Lucha, P., 2008. A sinkhole susceptibility
797 zonation based on paleokarst analysis along a stretch of the Madrid-Barcelona
798 high-speed railway built over gypsum- and salt-bearing evaporites (NE Spain).
799 Engineering Geology 102, 62-73.
800 Guerrero, J., Gutiérrez, F., Galve, J.P., 2013. Large depressions, thickened terraces, and
801 gravitational deformation in the Ebro River valley (Zaragoza area, NE Spain):
802 Evidence of glauberite and halite interstratal karstification. Geomorphology, 196,
803 162-176.
804 Gutiérrez, F., 2010. Hazards associated with karst. In: Alcantara, I., Goudie, A.S. (Eds.),
805 Geomorphological Hazards and Disaster Prevention. Cambridge University Press,
806 Cambridge, UK, pp. 161-175.
807 Gutiérrez, F., Cooper, A.H., 2002. Evaporite dissolution subsidence in the historical city
808 of Calatayud, Spain: Damage appraisal and prevention. Natural Hazards 25, 259-
809 288.
810 Gutiérrez, F., Galve, J.P., Guerrero, J., Lucha, P., Cendrero, A., Remondo, J., Bonachea,
811 J., Gutiérrez, M., Sánchez, J.A., Gutierrez, F., Gutierrez, M., Sanchez, J.A., 2007.
812 The origin, typology, spatial distribution and detrimental effects of the sinkholes
813 developed in the alluvial evaporite karst of the Ebro River valley downstream of
814 Zaragoza city (NE Spain). Earth Surface Processes and Landforms 32, 912-928.

Gutiérrez, F., Guerrero, J., Lucha, P., Gutierrez, F., 2008a. A genetic classification of sinkholes illustrated from evaporite paleokarst exposures in Spain. Environmental Geology 53, 993-1006.

Gutiérrez, F., Calaforra, J.M., Cardona, F., Ortí, F., Durán, J.J., Garay, P., 2008b. Geological and environmental implications of the evaporite karst in Spain. Environmental Geology 53, 951-965.

Gutiérrez, F., Galve, J.P., Lucha, P., Bonachea, J., Jordá, L., Jordá, R., 2009. Investigation of a large collapse sinkhole affecting a multi-storey building by means of geophysics and the trenching technique (Zaragoza city, NE Spain). Environmental Geology 58, 1107-1122.

Gutiérrez, F., Galve, J.P., Lucha, P., Castañeda, C., Bonachea, J., Guerrero, J., 2011. Integrating geomorphological mapping, trenching, InSAR and GPR for the identification and characterization of sinkholes: A review and application in the mantled evaporite karst of the Ebro Valley (NE Spain). Geomorphology 134, 144-156.

Herrera, G., Tomás, R., Lopez-Sanchez, J.M., Delgado, J., Vicente, F., Mulas, J., Cooksley, G., Sanchez, M., Duro, J., Arnaud, A., Blanco, P., Duque, S., Mallorqui, J.J., De la Vega-Panizo, R., Monserrat, O., 2009. Validation and comparison of Advanced Differential Interferometry Techniques: Murcia metropolitan area case study. ISPRS Journal of Photogrammetry and Remote Sensing 64, 501-512.

Hooper, A., Segall, P., Zebker, H., 2007. Persistent scatterer interferometric synthetic aperture radar for crustal deformation analysis, with application to Volcán Alcedo, Galápagos. Journal of Geophysical Research 112, B07407.

838 Koutepov, V.M., Mironov, O.K., Tolmachev, V.V., 2008. Assessment of suffusion-
839 related hazards in karst areas using GIS technology; Advances and challenges of
840 GIS and DBMS applications in karst. Environmental Geology 54, 957-962.
841 Lei, M., Jiang, X., Yu, L., 2002. New advances in karst collapse research in China.
842 Environmental Geology 42, 462-468.
843 Massonnet, D., Feigl, K.L., 1998. Radar interferometry and its application to changes in
844 the Earth's surface. Reviews of Geophysics 36, 441-500.
845 Meisina, C., Zucca, F., Notti, D., Colombo, A., Cucchi, A., Savio, G., Giannico, C.,
846 Bianchi, M., 2008. Geological Interpretation of PSInSAR Data at Regional Scale.
847 Sensors 8, 7469-7492.
848 Mulas, J., Aragón, R., Martínez, M., Lambán, J., García-Arostegui, J., Fernández-Grillo,
849 A., Hornero, J., Rodríguez, J., Rodríguez, J., 2003. Geotechnical and hydrological
850 analysis of land subsidence in Murcia (Spain), Proc. of the 1st International Conf.
851 on Groundwater in Geotechnical Engineering, RMZ-M&G, Bled, Slovenia, pp.
852 249-252.
853 Nof, R.N., Baer, G., Ziv, A., Raz, E., Atzori, S., Salvi, S., 2013. Sinkhole precursors
854 along the Dead Sea, Israel, revealed by SAR interferometry. Geology 41, 1019-
855 1022.
856 Paine, J.G., Buckley, S.M., Collins, E.W., Wilson, C.R., Box, X., 2012. Assessing
857 Collapse Risk in Evaporite Sinkhole-prone Areas Using Microgravimetry and
858 Radar Interferometry. Journal of Environmental & Engineering Geophysics 17,
859 75-87.
860 Paukstys, B., Cooper, A.H., Arustiene, J., 1999. Planning for gypsum geohazards in
861 Lithuania and England. Engineering Geology 52, 93-103.

862 Pueyo-Anchuela, O., Pocoví-Juan, A., Casas-Sainz, A.M., Ansón-López, D., Gil-Garbi,
863 H., 2013. Actual extension of sinkholes: Considerations about geophysical,
864 geomorphological, and field inspection techniques in urban planning projects in
865 the Ebro basin (NE Spain). Geomorphology 189, 135-149.
866 Quirantes, J., 1978. Estudio sedimentológico y estratigráfico del Terciario continental
867 de los Monegros. Zaragoza, ed. Institución Fernando El Católico (CSIC),
868 Diputación Provincial de Zaragoza, 207 pp.
869 Rodríguez-Tribaldos, V., Gutiérrez, F., Green, A., Carbonel, D., Horstmeyer, H.,
870 Schmelzbach, C., *in press*. Characterizing sagging and collapse sinkholes in a
871 mantled karst by means of Ground Penetrating Radar (GPR). Environmental &
872 Engineering Geoscience.
873 Rosen, P.A., Hensley, S., Joughin, I.A.N.R., Li, F.U.K.K., Madsen, S.N., Member, S.,
874 Rodríguez, E., Goldstein, R.M., 2000. Synthetic Aperture Radar Interferometry.
875 88 pp.
876 Rucker, M., Panda, B., Meyers, R., Lommler, J., 2013. Using InSAR to detect
877 subsidence at brine wells, sinkhole sites, and mines. Carbonates and Evaporites 28,
878 141-147.
879 Salvany, J.M., 2009. Geología del yacimiento glauberítico de Montes de Torrero
880 (Zaragoza) 77 pp.
881 Salvany, J.M., García-Veigas, J., Ortí, F., 2007. Glauberite-halite association of the
882 Zaragoza Gypsum Formation (Lower Miocene, Ebro Basin, NE Spain).
883 Sedimentology 54, 443-467.
884 Sandwell, D., Myer, D., Mellors, R., Shimada, M., Brooks, B., Foster J., 2007.
885 Accuracy and Resolution of ALOS Interferometry: Vector Deformation Maps of

the Father's Day Intrusion at Kilauea. IEEE Trans. Geosci. Rem. Sens. 2007-00737.R1

Schäffer, U., 2009. Hamburg, Germany. In: R. Capes, S. Marsh (Eds.), The Terrafirma Atlas, A compendium of results produced by the European Space Agency GMES Service Element Project Terrafirma 2003-2009. ESRIN Contract 19366/05/I-EC, 23 p.

Simón, J.L., Soriano, M.A., Arlegui, L.E., Gracia, F.J., Liesa, C.L., Pocoví, A., 2008. Space-time distribution of ancient and active alluvial karst subsidence: examples from central Ebro Basin, Spain. Environmental Geology 53, 1057-1065.

Soriano, M.A., Simón, J.L., 2002. Subsidence rates and urban damages in alluvial dolines of the Central Ebro basin (NE Spain). Environmental Geology 42, 476-484.

Thierry, P., Prunier-Leparmentier, A.-M., Lembezat, C., Vanoudheusden, E., Vernoux, J.-F., 2009. 3D geological modelling at urban scale and mapping of ground movement susceptibility from gypsum dissolution: The Paris example (France). Engineering Geology 105, 51-64.

Tolmachev, V., Leonenko, M., 2011. Experience in collapse risk assessment of building on covered karst landscapes in Russia. In: Van Beynen, P. (Ed.), Karst Management. Springer, Dordrecht, New York, pp. 75-102.

Tomás, R., Márquez, Y., Lopez-Sanchez, J.M., Delgado, J., Blanco, P., Mallorquí, J.J., Martínez, M., Herrera, G., Mulas, J., 2005. Mapping ground subsidence induced by aquifer overexploitation using advanced Differential SAR Interferometry: Vega Media of the Segura River (SE Spain) case study. Remote Sensing of Environment, 98, 269-283.

910 Waltham, T., Bell, F.G., Culshaw, M.G., 2005. Sinkholes and Subsidence: karst and
911 cavernous rocks in engineering and construction. Springer & Praxis Publishing,
912 Chichester, UK, 416 pp.
913

Tables

Table 1. Sensor, date and orbit number of the SAR images used in this study. For each mission, the temporal interval refers to the time elapsed since the acquisition of the oldest image. D: descending mode; A: ascending mode.

ERS-1* /2 SAR			ENVISAT ASAR			ALOS PALSAR		
Date	Orbit (D)	Days	Date	Orbit (A)	Days	Date	Orbit (A)	Days
05/07/1995*	20766	0	02/05/2003	6124	0	12/02/2007	5614	0
10/08/1995	1594	36	15/08/2003	7627	105	30/06/2007	7627	138
14/09/1995	295	71	19/09/2003	8128	140	15/08/2007	8298	184
10/04/1996*	24774	280	02/01/2004	9631	245	30/09/2007	8969	230
20/06/1996	6103	351	06/02/2004	10132	280	31/12/2007	10311	322
29/08/1996	7105	421	12/03/2004	10633	315	01/04/2008	11653	414
03/10/1996	7606	456	21/05/2004	11635	385	17/05/2008	12324	460
12/12/1996	8608	526	25/06/2004	12136	420	02/07/2008	12995	506
20/02/1997	9610	596	30/07/2004	12637	455	20/08/2009	19034	920
27/03/1997	10111	631	08/10/2004	13639	525	05/10/2009	19705	966
01/05/1997	10612	666	17/12/2004	14641	595	05/01/2010	21047	1058
10/07/1997	11614	736	21/01/2005	15142	630	20/02/2010	21718	1104
18/09/1997	12616	806	06/05/2005	16645	735	07/04/2010	22389	1150
27/11/1997	13618	876	15/07/2005	17647	805			
05/02/1998	14620	946	19/08/2005	18148	840			
03/09/1998	17626	1156	28/10/2005	19150	910			
01/04/1999	20632	1366	02/12/2005	19651	945			
10/06/1999	21634	1436	10/02/2006	20653	1015			
14/07/1999*	41808	1470	26/05/2006	22156	1120			
27/01/1999*	43311	1575	30/06/2006	22657	1155			
28/10/1999	23638	1576	06/04/2007	26665	1435			
06/01/2000	24640	1646	20/07/2007	28168	1540			
09/02/2000*	44814	1680	15/02/2008	31174	1750			
16/03/2000	25642	1716	21/03/2008	31675	1785			
03/08/2000	27646	1856	04/07/2008	33178	1890			
12/10/2000	28648	1926	04/06/2010	43198	2590			
21/12/2000	29650	1996	09/07/2010	43699	2625			
			13/08/2010	44200	2660			
			17/09/2010	44701	2695			

923 **Figure captions**

924

925 Figure 1. (a) Regional geological setting of the Ebro Valley, showing the main outcrops
926 of evaporite rocks in NE Spain. The Zaragoza Gypsum Formation is highlighted with a
927 grey dashed line (modified from Gutiérrez et al., 2008b). (b) Geographical distribution
928 of the study area and the DInSAR velocity maps depicted on a shaded digital elevation
929 model. (c) Map of the study area illustrating the main built-up areas and infrastructures.

930

931 Figure 2. Analyzed sinkhole typologies. Images (a), (b) and (c) illustrate the surface
932 morphology of large depressions, large collapse sinkholes and small collapse sinkholes,
933 respectively. Approximate scale is indicated. (d) Schematic sections showing the
934 internal geometry and subsidence mechanism of the different sinkhole types. (e, f , g)
935 Exposures in railway cuttings showing paleosinkholes. (e) Cover and bedrock sagging
936 paleosinkhole. Note the tilted evaporitic bedrock strata on the left side of the synform.
937 (f) Collapse structure in the evaporite bedrock bounded by well-defined failure planes
938 (arrows). The gypsum bedrock underlying the alluvium in the foundered block has been
939 transformed into a collapse breccia. (g) Solutionally-enlarged joint filled with alluvium
940 by downward migration derived from a pre-existing detrital cover.

941

942 Figure 3. Distribution of the mean LOS displacement rate values obtained from C-band
943 (left) and L-band (right) data. The higher dispersion of the L-SPN values is related to
944 the lower level of signal to noise ratio of the ALOS data. Each frequency curve is
945 normalized to the number of points of the corresponding velocity maps. Dashed lines
946 indicate the minimum LOS displacement values considered to represent actual ground
947 deformation. The curves of the L-SPN-map depict the frequency distribution of the

948 measured values and the corrected ones by subtracting 1 mm/yr to all the mean LOS
949 displacement values.
950
951 Figure 4. Sinkhole map and DInSAR velocity maps. The zoomed portions correspond to
952 the sector of the Europa and El Portazgo industrial estates next to the N-232 highway.
953 The UTM coordinate system ED195030N is used in this figure and the remaining
954 figures.
955
956 Figure 5. C-SPN-map on an orthoimage from 2009 showing subsidence within a factory
957 located in the Europa industrial estate. Dashed white lines are the boundaries of the
958 sinking centers mapped by Simón et al. (2008). Right-bottom insert: Aerial photograph
959 of the sudden collapse (6 m deep) occurred on 1999.
960
961 Figure 6. (a) Sector of Utebo village where C-SPN-map indicates subsidence associated
962 to a sinkhole inventoried by Galve et al. (2009b) (dashed line). These authors
963 characterized this sinkhole as inactive applying traditional methods. (b) and (c) Open
964 joints and undermined structures associated to the subsidence feature represented in (a).
965
966 Figure 7. L-SPN- (left) and C-SPN- (right) maps on 2009 orthoimages. Dashed white
967 lines depict the boundaries of an active sinkhole inventoried by Galve et al. (2009). See
968 figure 4d and f for the location of this area.
969
970 Figure 8. (a) Orthoimage taken in 2009 showing the location of a collapse sinkhole
971 occurred on May 24, 2006 (see c) and subsidence detected in an adjacent factory by the
972 C-SPN-map. The location of the site is indicated in figure 4d. (b) LOS displacement

973 time series corresponding to the building adjacent to the collapse. (c) Sudden collapse
974 sinkhole occurred on May 24, 2006 and photographed the day after.
975
976 Figure 9. L-SPN- (a) and C-SPN- (b) deformation data on an orthoimage from 2009 in
977 Sinkhole A1 (dashed line). (c) LOS displacement profile 2 extracted from the C-SPN
978 map. The extent of the inventoried sinkhole within the profile is indicated by the shaded
979 area. The location of the profile is shown in (b).
980
981 Figure 10. C-SPN-map deformation data on an orthoimage from 2009 in the area of
982 sinkholes A2 and A3.
983
984 Figure 11. Subsidence recorded by the C-SPN-map on the margins of sinkhole B1,
985 located in Valdefierro suburb (left). In this case, the topographic expression of the
986 sinkhole has not been completely obliterated by the accumulation of anthropogenic
987 deposits and construction, as illustrates the 5 x 5 m LiDAR DEM of the Instituto
988 Geográfico Nacional (right).
989
990 Figure 12. The C-SPN-map shows subsidence only in the western sector of Sinkhole B2
991 (white dashed line in left image), probably because subsidence rates reach values higher
992 than the maximum measurable displacement rate, as supports the distribution of damage
993 in the buildings located in the eastern sector of the sinkhole (right).
994
995 Figure 13. Examples of structural damage within Sinkhole B2. Fissures (A), cracks (B)
996 and open joints (D) observed in building walls. Road affected by fissures and scarplets
997 (C). Traffic sign tilted (E and F) towards the main sinking centre of the area.

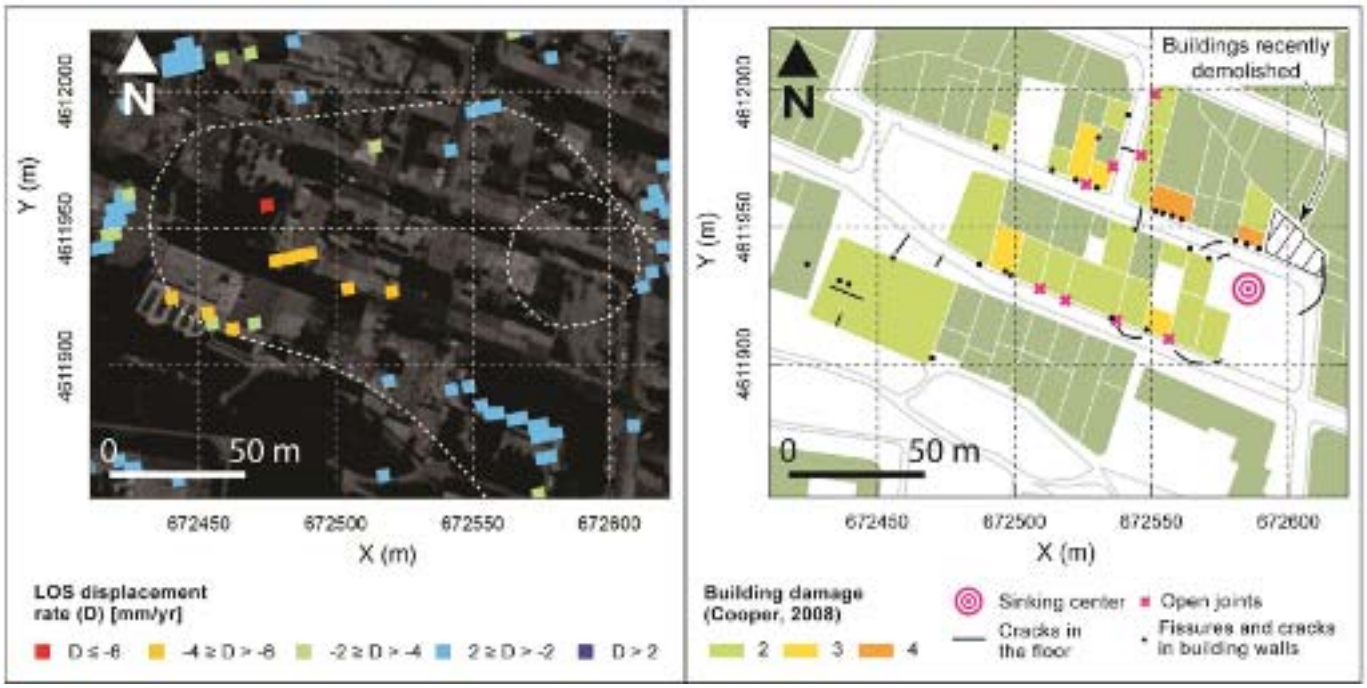
N
Y (m)
4612000
4611950
4611900
0
50 m
672450
672500
672550
672600
X (m)
LOS displacement rate (D) [mm/yr]
D ≤ -6
-4 ≥ D > -6
-2 ≥ D > -4
2 ≥ D > -2
D > 2
Buildings recently demolished
Building damage (Cooper, 2008)
2
3
4
Sinking center
Open joints
Cracks in the floor
Fissures and cracks in building walls


A
B
C
D
E
F

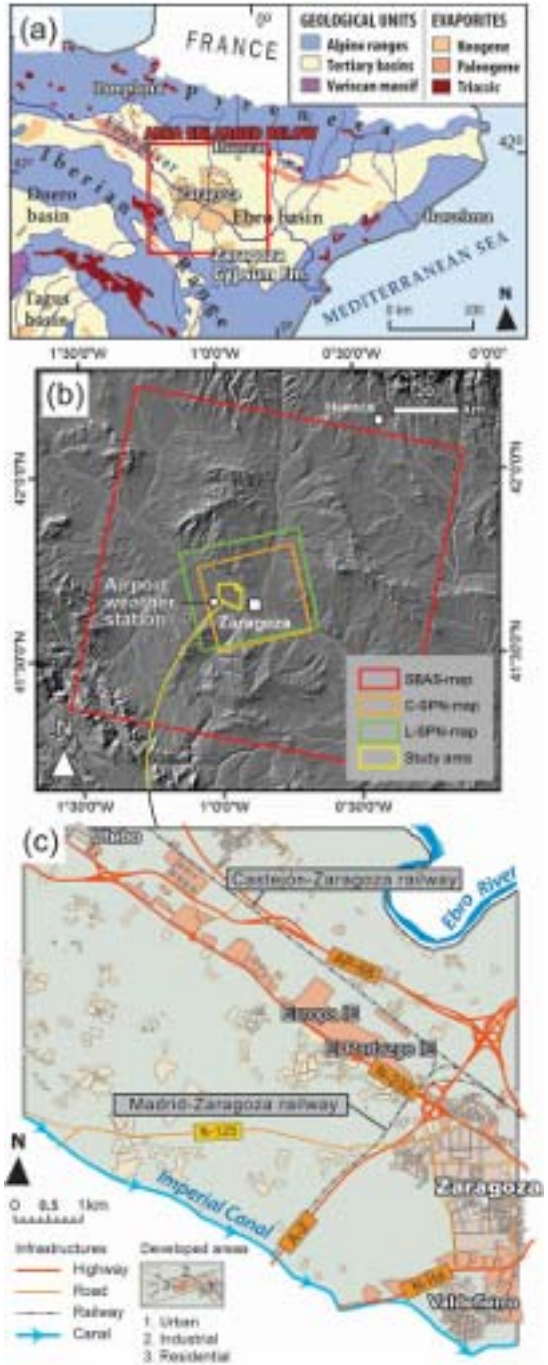
(a)
FRANCE
GEOLOGICAL UNITS
Alpine ranges
Tertiary basins
Variscan massif
EVAPORITES
Neogene
Paleogene
Triassic
Iberian
Ebro basin
Ebro basin
Pyrenean
Catalan
MEDITERRANEAN SEA
Tagus basin
(b)
Airport weather station
Zaragoza
SBAS-map
C-SPN-map
L-SPN-map
Study area
(c)
Castellón-Zaragoza railway
Ebro River
Madrid-Zaragoza railway
Imperial Canal
Zaragoza
Infrastructures
Highway
Road
Railway
Canal
Developed areas
1. Urban
2. Industrial
3. Residential

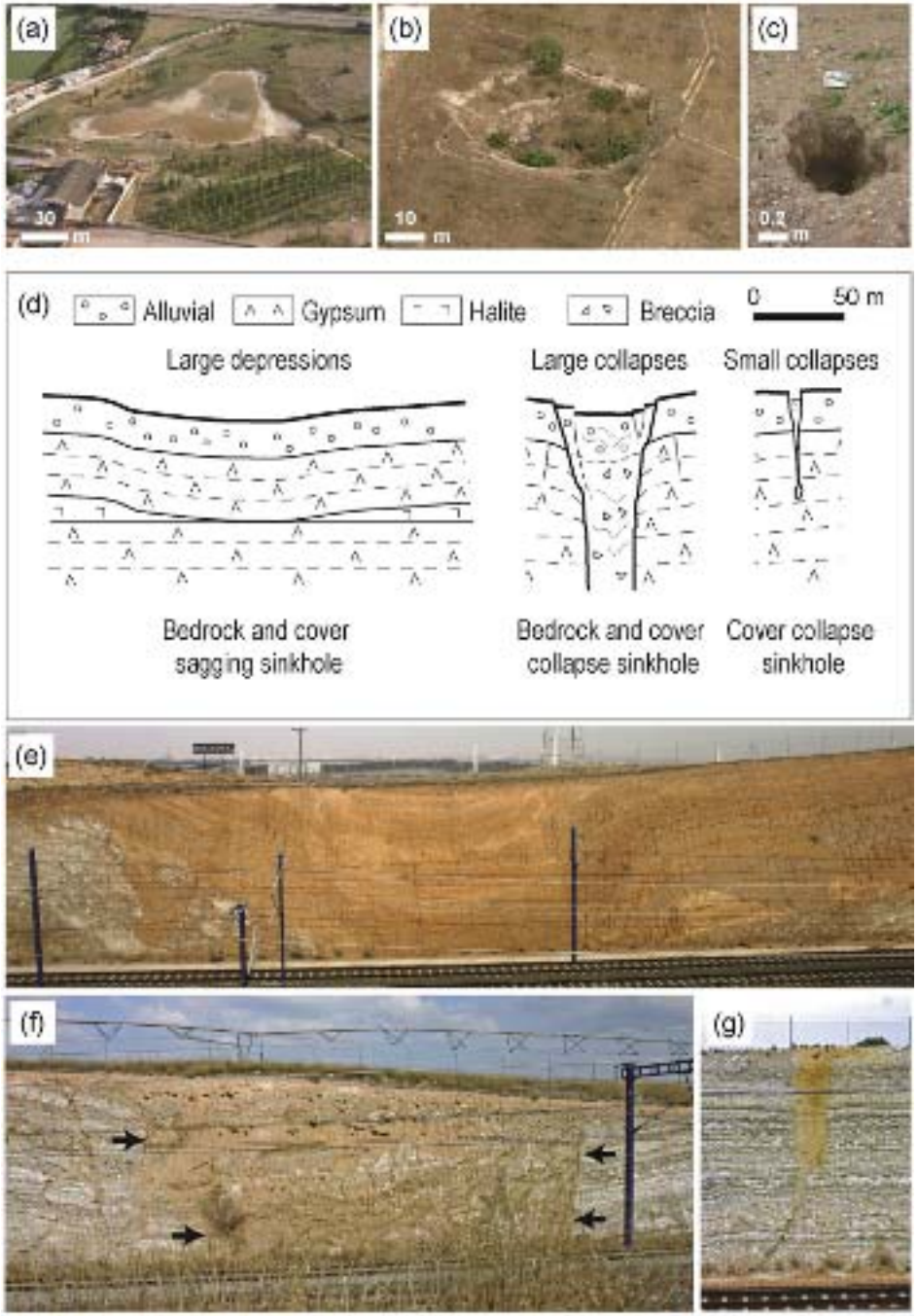
(a)
30 m
(b)
10 m
(c)
0.2 m
(d)
Alluvial
Gypsum
Halite
Breccia
0
50 m
Large depressions
Large collapses
Small collapses
Bedrock and cover sagging sinkhole
Bedrock and cover collapse sinkhole
Cover collapse sinkhole
(e)
(f)
(g)

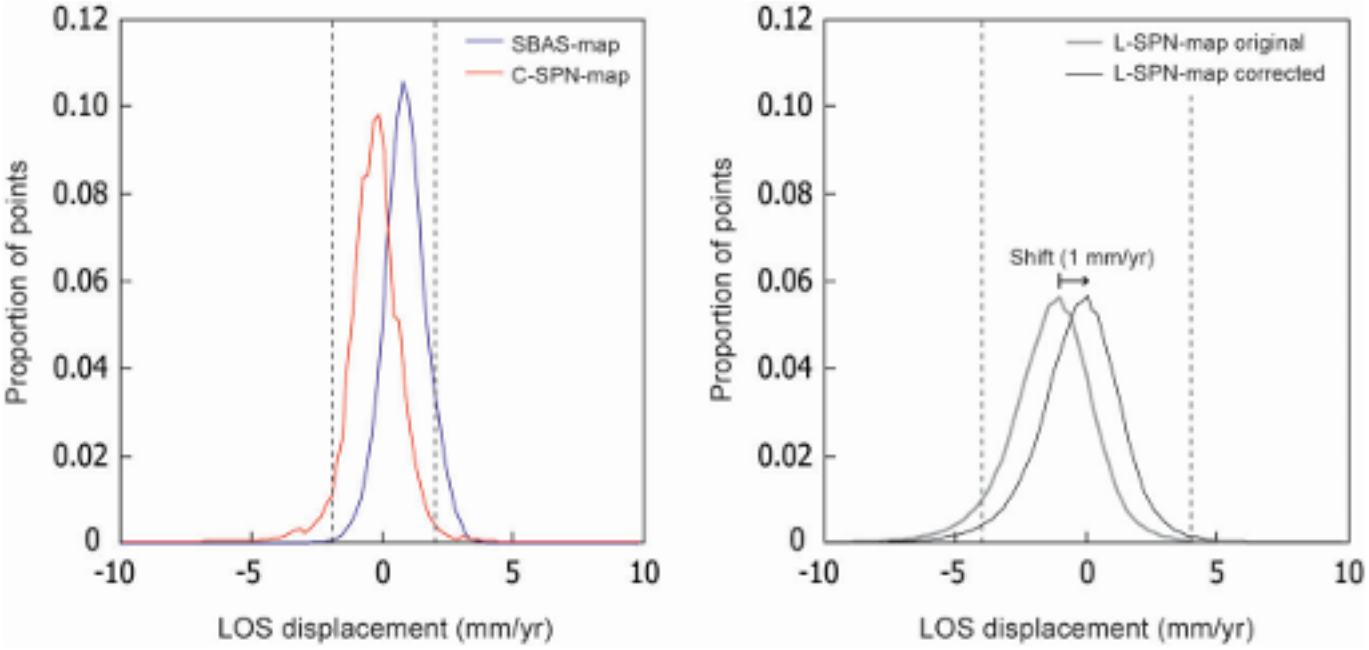
0.12
0.10
0.08
0.06
0.04
0.02
0
Proportion of points
SBAS-map
C-SPN-map
-10
-5
0
5
10
LOS displacement (mm/yr)
L-SPN-map original
L-SPN-map corrected
Shift (1 mm/yr)

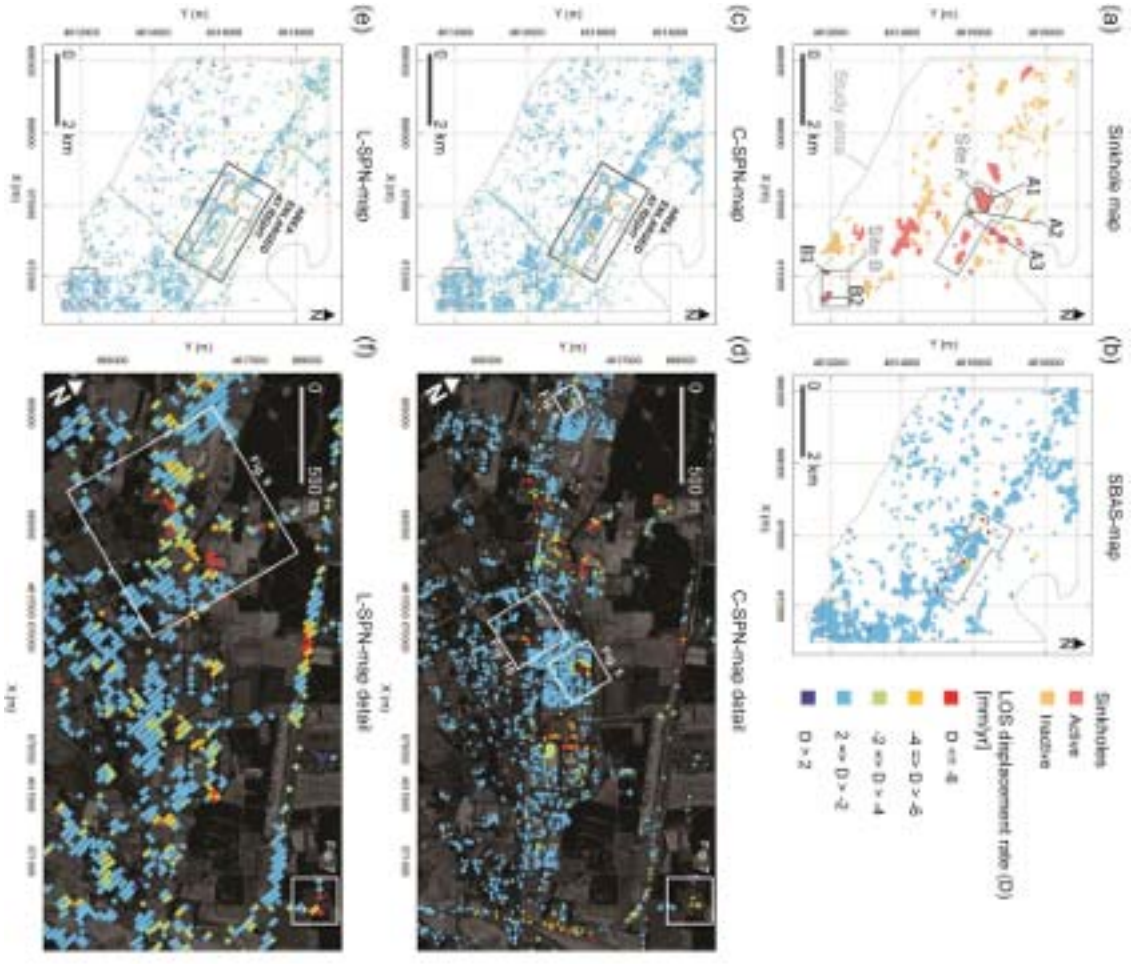
(a)
(b)
(c)
(d)
(e)
(f)
Sinkhole map
SBAS-map
C-SPN-map
L-SPN-map
C-SPN-map detail
L-SPN-map detail
Study area
Site A
Site B
A1
A2
A3
B1
B2
2 km
500 m
N
Y (m)
X (m)
Sinkholes
Active
Inactive
LOS displacement rate (D) [mm/yr]
D <= -6
-4 => D > -6
-2 => D > -4
2 => D > -2
D > 2

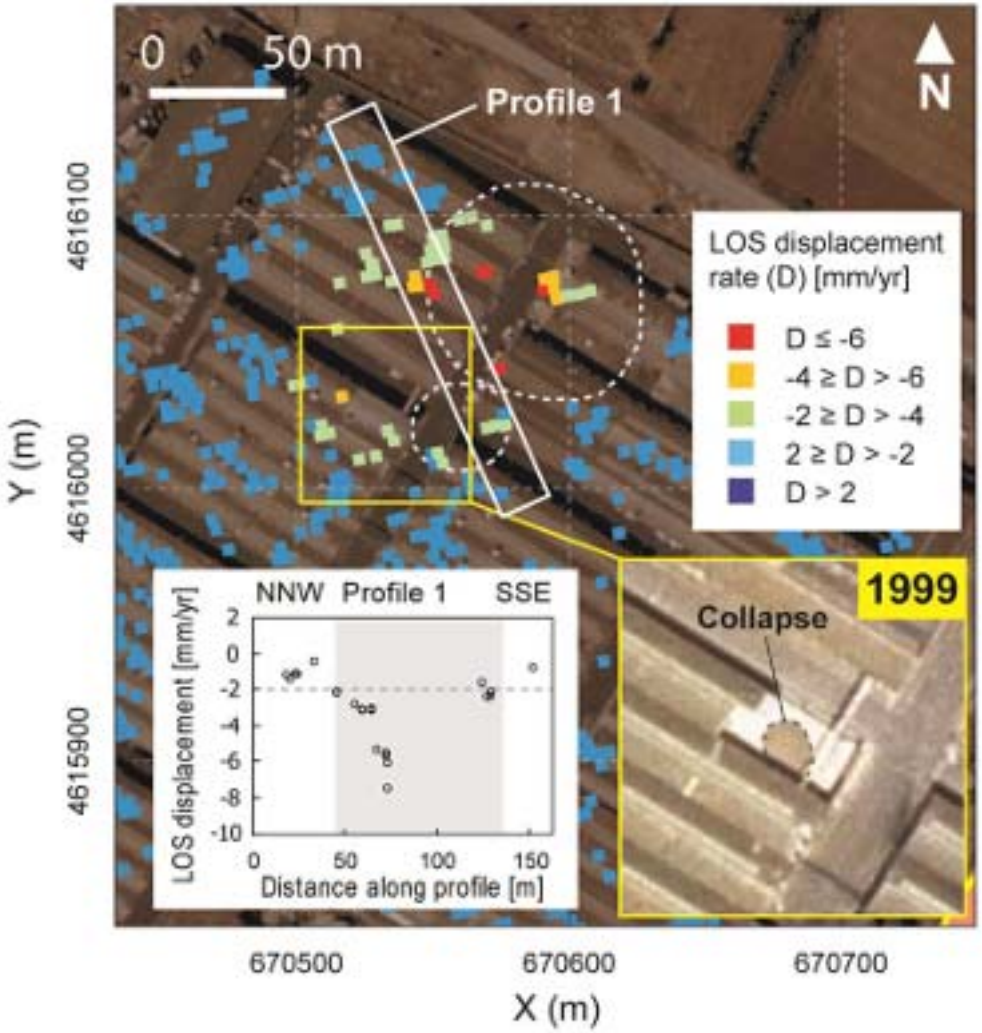
0
50 m
Profile 1
N
LOS displacement rate (D) [mm/yr]
D ≤ -6
-4 ≥ D > -6
-2 ≥ D > -4
2 ≥ D > -2
D > 2
NNW Profile 1 SSE
LOS displacement [mm/yr]
Distance along profile [m]
1999
Collapse
Y (m)
4616100
4616000
4615900
670500
670600
670700
X (m)

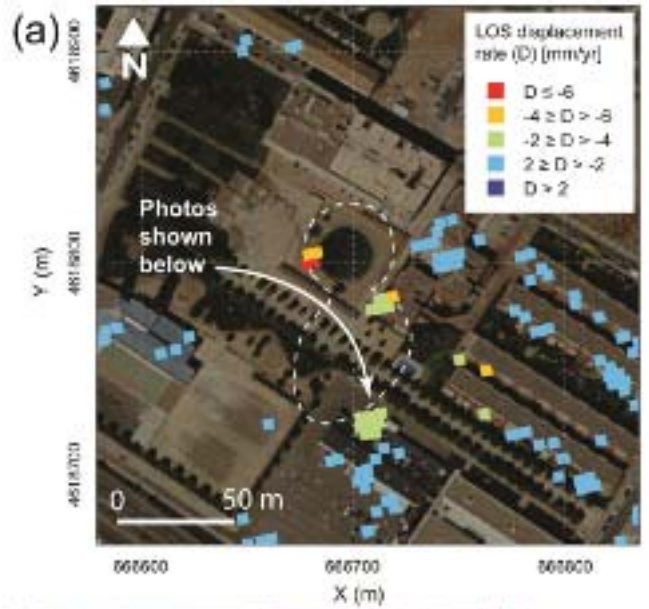
(a)
N
LOS displacement rate (D) [mm/yr]
D ≤ -6
-4 ≥ D > -6
-2 ≥ D > -4
2 ≥ D > -2
D > 2
Photos shown below
0
50 m
Y (m)
X (m)


(b)


(c)

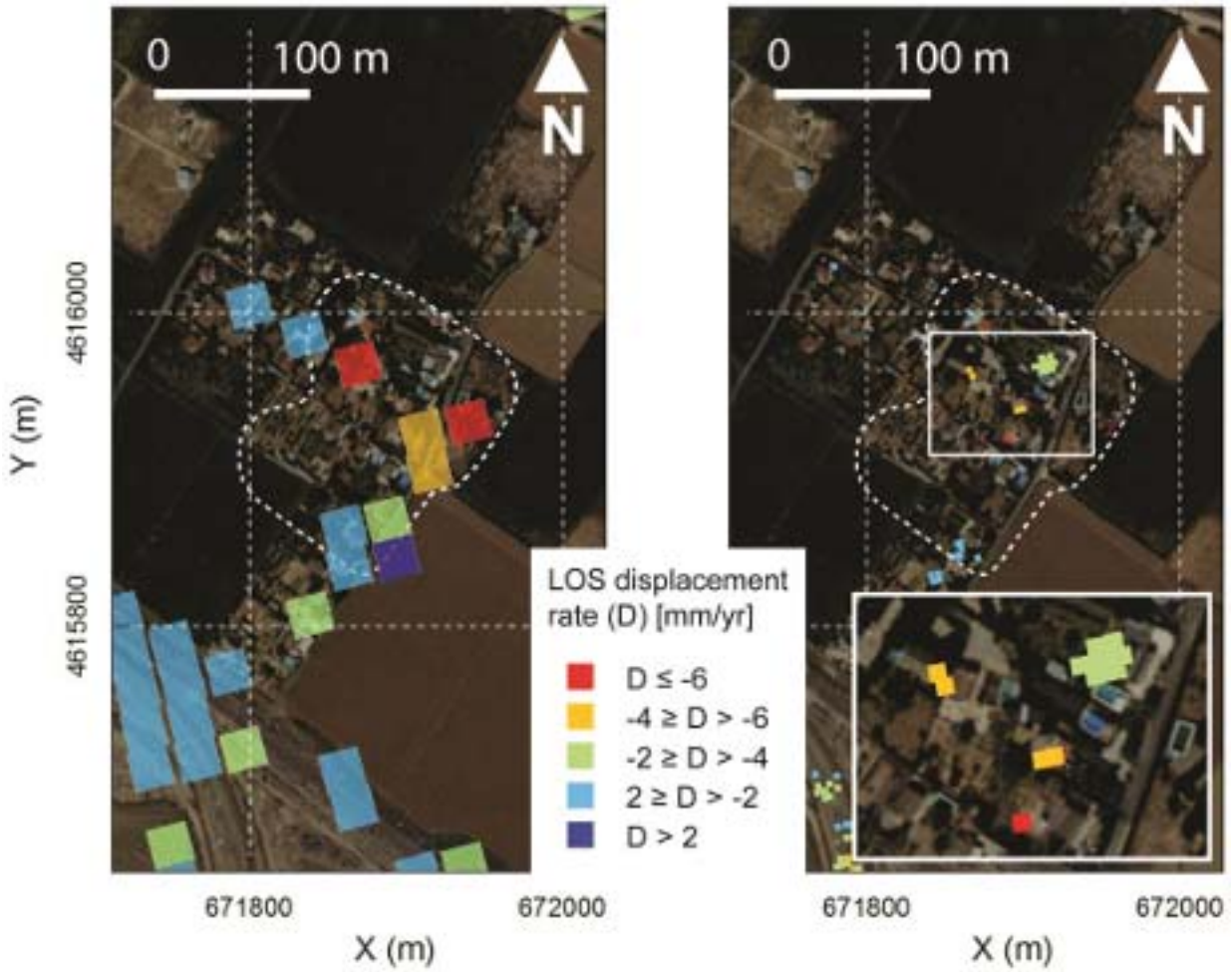
0
100 m
N
4616000
4615800
Y (m)
LOS displacement rate (D) [mm/yr]
D ≤ -6
-4 ≥ D > -6
-2 ≥ D > -4
2 ≥ D > -2
D > 2
671800
672000
X (m)

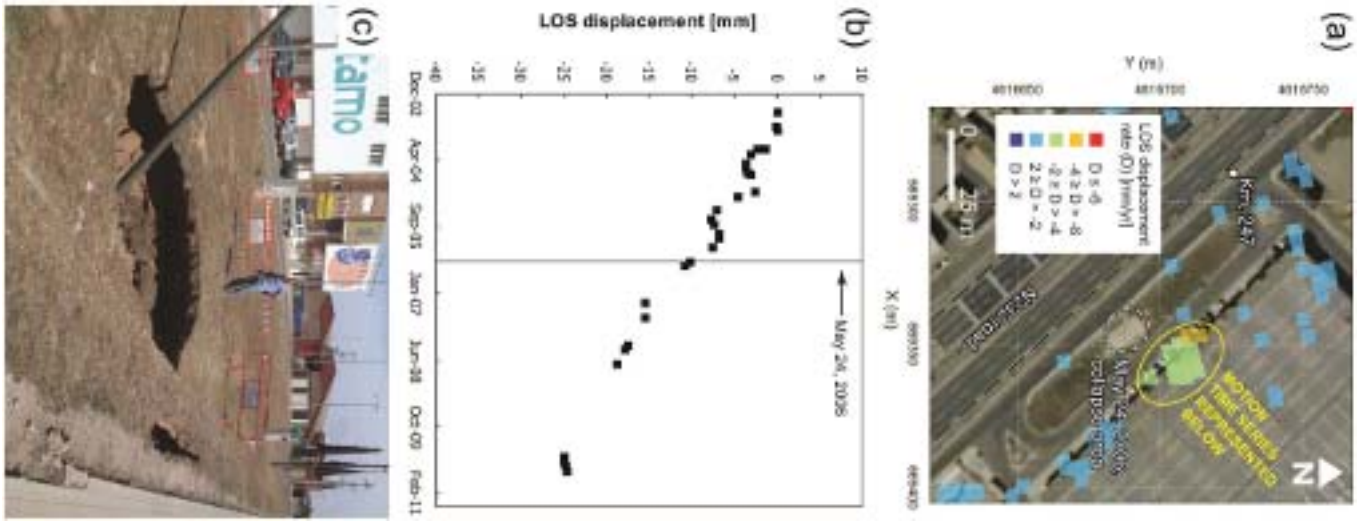
(a)
(b)
LOS displacement [mm]
May 24, 2006
(c)
Arno

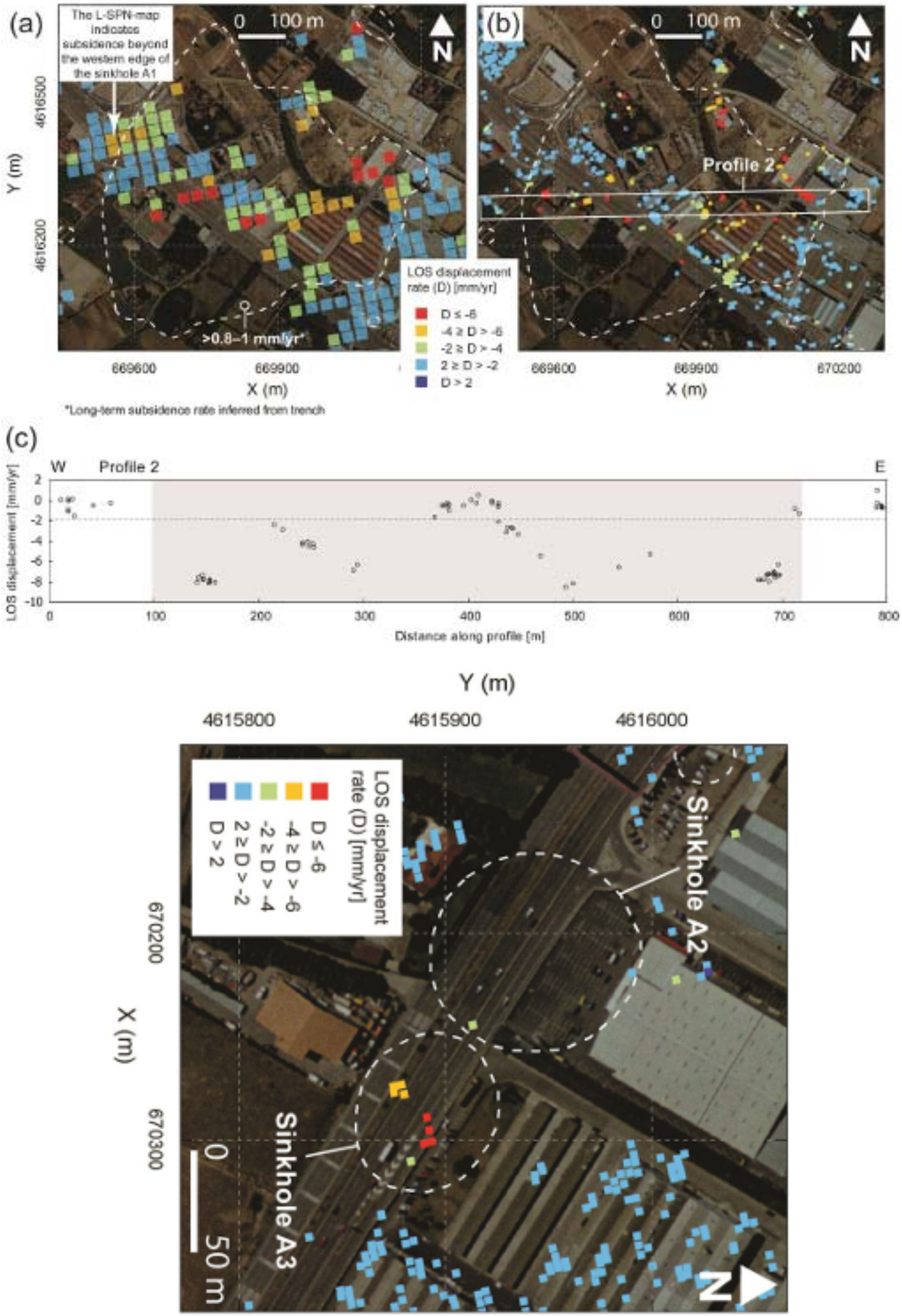
(a)
The L-SPN-map indicates subsidence beyond the western edge of the sinkhole A1
0 100 m
N
>0.8–1 mm/yr*
(b)
0 100 m
N
Profile 2
LOS displacement rate (D) [mm/yr]
D ≤ -6
-4 ≥ D > -6
-2 ≥ D > -4
2 ≥ D > -2
D > 2
Y (m)
4616500
4616200
669600
669900
X (m)
669600
669900
670200
X (m)
*Long-term subsidence rate inferred from trench
(c)
W
Profile 2
E
LOS displacement [mm/yr]
2
0
-2
-4
-6
-8
-10
0
100
200
300
400
500
600
700
800
Distance along profile [m]
Y (m)
4615800
4615900
4616000
LOS displacement rate (D) [mm/yr]
D ≤ -6
-4 ≥ D > -6
-2 ≥ D > -4
2 ≥ D > -2
D > 2
Sinkhole A2
Sinkhole A3
X (m)
670200
670300
0
50 m
N

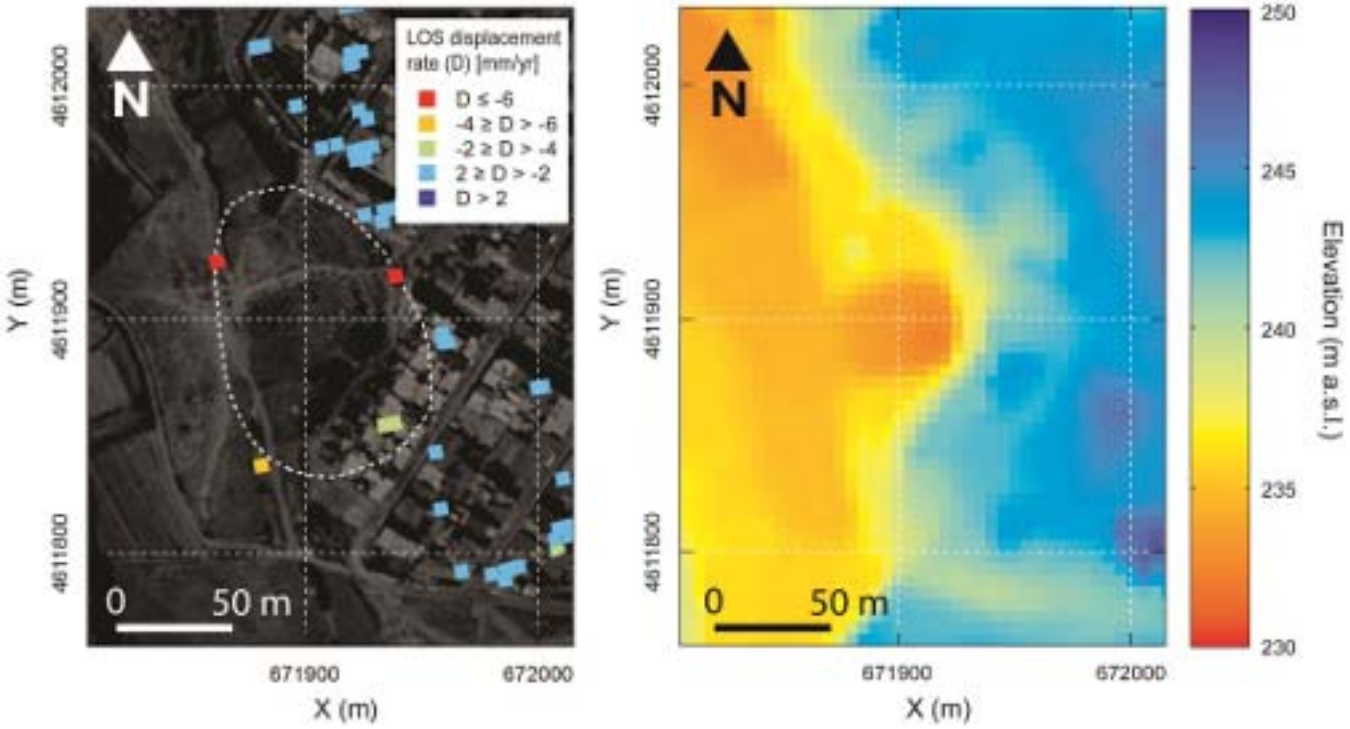
LOS displacement rate (D) [mm/yr]
D ≤ -6
-4 ≥ D > -6
-2 ≥ D > -4
2 ≥ D > -2
D > 2
N
0
50 m
4612000
4611900
4611800
Y (m)
671900
672000
X (m)
Elevation (m a.s.l.)
250
245
240
235
230

Table S1. Main characteristics of the SAR datasets and DInSAR deformation maps: The information of the DInSAR deformation maps refers to the whole area covered by them (see Fig. 1b).

	SBAS-map	C-SPN-map	L-SPN-map
SAR acquisition			
Band / Polarisation	C / VV	C / VV	L / HH
Wavelength [cm]	5.6	5.6	23.6
Incidence angle	23	23	38.7
Revisiting period [days]	35	35	46
Orbital track / Frame	237 / 2766	58 / 829	665 / 820
Acquisition geometry	Descending	Ascending	Ascending
Pixel size [m] radar geometry	4 x 10	4 x 10	8 x 4
Data set period	07/1995–12/2000 (5.47 yrs)	05/2003–09/2010 (7.38 yrs)	02/2007–04/2010 (3.15 yrs)
Temporal span between two acquisitions [days]			
Mean	87	96	96
Maximum	274	700	414
Minimum	34	5	46
SAR processing			
Number of SAR images	27	29	13
Number of interferograms	74	61	78
Maximum spatial baseline [m]	300	138	393
Maximum temporal baseline [days]	1400	1050	1150
DEM (pixel size)	SRTM (90 m)	GIS Oleícola (20 m)	GIS Oleícola (20 m)
Coherence threshold	0.75	0.46	0.40
Deformation maps			
Area [km^2]	10035	763	1097
No. of measurement points	172582	282152	222747
Type of point	Pixel (~90 m)	Persistent scatterer	Pixel (~25 m)
Density of measurement points [points/km^2]	17.2	369.8	203.1
LOS displacement rate [mm/yr]			
Mean	-1	-0.2	-0.2
Maximum value (uplift)	8	10	7
Minimum value (subsidence)	-17	-10	-10
standard deviation	0.8	1.1	1.7
Cumulative LOS displacement [mm]			
Mean	1.2	-1.8	-0.2
Maximum value (uplift)	32	81	24
Minimum value (subsidence)	-94	-86	-31
standard deviation	5.4	8.0	4.9

Table S2. Main characteristics of the sinkholes and InSAR data for the study area and representative sites. LC: Large Collapses; LD: Large Depressions.

	Study area			**Site A (N232 Road)**			**Site B (Valdefierro suburb)**		
Area [km^2]	40.8			2.15			0.75		
No. of inventoried sinkholes[(1)]	158 (58 LC and 100 LD)			18 (12 LC and 6 LD)			4 (3 LC and 1 LD)		
No. of inventoried active sinkholes[(1)]	48 (34 LC and 14 LD)			11 (6 LC and 5 LD)			4 (3 LC and 1 LD)		
Area of sinkholes [km^2]	3.35			0.46			0.05		
Area affected by active sinkholes [km^2]	1.06			0.43			0.05		
Area affected by active sinkholes [%]	2.6%			20.0%			6.6%		
Deformation maps	SBAS-map	C-SPN-map	L-SPN-map	SBAS-map	C-SPN-map	L-SPN-map	SBAS-map	C-SPN-map	L-SPN-map
No. of measurement points	1057	24372	6348	102	2948	544	84	1868	360
No. of subsidence points[(2)]	16	1772	447	10	1879	53	16	103	0
Density of measurement points [points/km^2]	26	597	156	47	1371	253	112	2491	480
Density of subsidence points[(2)] [points/km^2]	0.4	43	11	5	874	25	21	137	0
LOS displacement rate [mm/yr]									
Mean	0.5	-0.7	-0.6	-0.2	-1.3	-1.7	0.2	-0.8	0.5
Maximum subsidence value	-17	-10	-10	-16	-10	-10	1	-9	-4
Standard deviation	1.1	1.2	1.7	2.6	1.7	1.8	0.4	0.9	0.9
Cumulative LOS displacement [mm]									
Mean	-1.5	-4.9	-1.3	-4.9	-9.3	-4.5	-2.3	-5.1	2.2
Maximum subsidence value	-94	-79	-29	-94	-75	-28	-9	-63	12
Standard deviation	6.1	8.4	5.0	14.1	12.5	5.2	3.1	6.6	3.1
No. of detected active sinkholes	2 LD	12 (6 LC, 6 LD)	10 (3 LC, 7 LD)	2 LD	5 (2 LC, 3 LD)	6 (2 LC, 4 LD)	0	2 (1 LC, 1 LD)	0
Area of the detected sinkholes [km^2]	0.33	0.48	0.54	0.30	0.34	0.35	0.00	0.03	0.00
Area of the detected sinkholes [%]	31%	45%	51%	70%	79%	81%	0%	60%	0%
No. of sinkholes revised as active	0	3 (2 LC, 1 LD[(3)])	1 LD	0	1 LC	0	0	1 LD[(3)]	0
No. of sinkholes discovered	0	2 LC	0	0	0	0	0	0	0

[(1)] The 39 inventoried small collapse sinkholes have not been considered. The sinkhole database of Galve et al. (2009a) has been updated and modified for the purposes of this work. Large collapses nested in large depressions have been included in the latter ones.

[(2)] Points with negative values. Negative values within the detection limits of the technique measurement (from 0 to -2 for C band and from 0 to -4 for L-band) are excluded.

[(3)] Previously defined inactive sector of the depression revised as active (see Figs. 12 and 13).

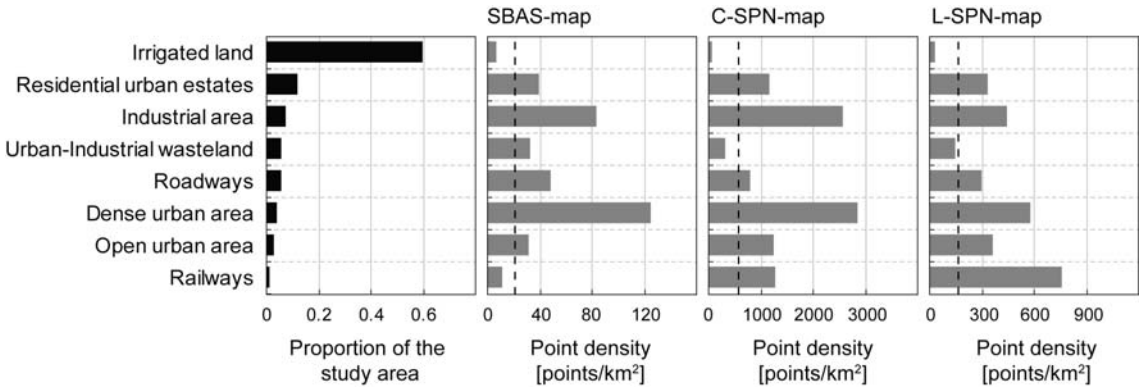

Figure S1. Proportion of the study area occupied by different land covers and density of measurement points for the different land covers in each DInSAR map. Vertical dashed lines indicate the overall density of points in the study area.